OPTICAL EMISSION SPECTROSCOPY OF LASER INDUCED PLASMAS CONTAINING CARBON AND TRANSITIONAL METALS

By

David Edmond Motaung

A thesis submitted for the completion of the requirements for the degree of Magister Scientiae in the Department of Physics, University of the Western Cape

Supervisor: Mr. Mathew Moodley, Council for Scientific and Industrial Research (CSIR)

Co-supervisor: Prof. Dirk Knoesen, University of the Western Cape (UWC)

December 2007

DEDICATED TO

My late Grandmother and My Uncle:

Motaung-Tshabalala Mamaburu .F and Motaung Machine Pholo.

For their unconditional love, support and encouragement.

David Motaung **December 2007**

ACKNOWLEDGEMENTS

- **Firstly I would like to THANK THE GOD ALMIGHTY for making this work possible.**

- **Secondly, I would like to THANK the following People who made this work to be a success:**

  - My sincere gratitude should be extended to my supervisor: Mr Mathew Moodley, Council for Scientific Industrial Research. I really appreciated his continuous support, supervision, guidance and valuable discussions and the technical work he taught me.

  - Special thank goes to my Co-Supervisor: Prof. Dirk Knoesen (UWC), I am extremely thankful for his support, vital discussions and his warm supervision.

  - Other special thanks go to Dr Gerald Malgas (CSIR), Dr. Chris Adrense (CSIR) and Franscious Cummings (CSIR), for their support, guidance and vital discussions.

  - I would also like to say thanks to the Staff of Physics Department at UWC: Prof. R. Lindsay, Prof. R. Madjoe, Prof. D. Adams, Prof. D. Marshall, Prof. I. Krylov, Dr. R. E. Julies, Dr. B A. Julies, Dr S. Halindintwali, Ms. A. Adams, Late Dr. T. K. Marais, Mr. Theo Muller, and the former lectures: Dr. R. Nchodu

and Dr. Shaun Wyngaardt for their diverse support that they provided me throughout these years and their trust.

- The staff of the Materials Research Group at iThemba LABS for their assistance during my Honours programme.

- I also owe a “thank you” to my fellow students, friends and colleagues at UWC, Home and CSIR: Clive, Gebhu, Teboho, Mzi, Patrick, Tlhogi, Dr. Pillai, Sarah, Elizabeth, Bonex, Thomas, Randall, Henry, Hlony, Tieho, Mlulami, Motsoeneng Tebello, Mamzizi, Moipone, Keiso, etc. for their continuous support.

- I am deeply grateful to my Mother: Ntswaki, Brothers and Sisters: Jimmy, Sello, Tankiso, Mookgo, Dikomo, Mpho, Dikomo and Lindiwe for their love, encouragement and moral support.

- Mpho for your ceaseless love, support you provided me throughout…and the blessed Omolemo Brandon Motaung.

- I would like to say Thanks to my Grand-grandma: Mambeko; my late Grand-Fathers: Ntate Titiya John and Nthea Jonas for raising me up, inspiring me to study and for their continuous love.

- Finally, I acknowledge the financial support of the CSIR, National Research Foundation (NRF), UWC and iTHEMBA LABS.

DECLARATION

I declare that

‘‘OPTICAL EMISSION SPECTROSCOPY OF LASER INDUCED PLASMAS CONTAINING CARBON AND TRANSITIONAL METALS”

is my own work and all the sources have been acknowledged by means of references.

David Edmond Motaung **December 2007**

Signature:_____

KEYWORDS

‘‘OPTICAL EMISSION SPECTROSCOPY OF LASER INDUCED PLASMAS CONTAINING CARBON AND TRANSITIONAL METALS”

Single-wall Carbon Nanotubes

Multi-wall Carbon Nanotubes

Laser Ablation

Optical Emission Spectroscopy

Laser Induced Plasmas

Raman Spectroscopy

Scanning Electron Microscopy

Transmission Electron Microscopy

David Motaung **December 2007**

ABSTRACT

‘‘OPTICAL EMISSION SPECTROSCOPY OF LASER INDUCED PLASMAS CONTAINING CARBON AND TRANSITIONAL METALS”

By

David Edmond Motaung

In situ optical emission spectroscopic studies on carbon plasma containing transitional metals by laser-furnace method of synthesizing carbon nanotubes have been carried out. The target was ablated by 1064 and 532 nm laser pulses at a furnace temperature of 1000 ºC in argon gas using different pressures and flow rates. The emission spectra of the plasma plume were registered with the use of an Andor spectrograph and an Andor iStar ICCD camera. The C_2 Swan bands and Deslandres systems were observed in the plasma emission spectra together with various ionization stages of Carbon, Yttrium and Nickel were also observed. The temperature measurements were performed by applying Boltzmann’s distribution law using singly ionized C (II) lines, while the density measurements were made by using the Stark broadening method. At a pressure of 400 Torr and flow rate 200 sccm, the initial temperature and electron density of 16 330 K and 2.15 $\times 10^{17}$ cm^{-3} were measured. The temporal and spatial behaviour of the electron temperature and density in the laser-generated plasma plume were analysed. The time evolutions of the temperature and density were found to decay adiabatically at earlier times in the lifetime of the plume. The spatial variation of electron density followed approximately 1/z dependence.

The spectroscopic, SEM and Raman measurements on carbon nanotubes under the exact conditions of which OES analysis were made showed that at a pressure of 400 Torr and a flow rate of 200 sccm, the quality and quantity of single-walled carbon nanotubes was the highest.

LIST OF ABBREVIATIONS

LA	:	Laser ablation
CVD	:	Chemical vapour deposition
TCVD	:	Thermal chemical vapour deposition
HWCVD	:	Hot wire chemical vapour deposition
PECVD	:	Plasma enhanced chemical vapour deposition
LACVD	:	Laser assisted chemical vapour deposition
ICCD	:	Intensified coupled charge Device
CNT	:	Carbon nanotube
SWCNTs	:	Single walled carbon nanotubes
MWCNTs	:	Multi walled carbon nanotubes
mg	:	milligram
cm	:	centimeters
mbar	:	millibar
min	:	minutes
s	:	seconds
sccm	:	standard cubic centimeters
MCP	:	Micro-channel plate
DDG	:	Digital delay generator
OES	:	Optical emission spectroscopy
EM	:	Electron microscopy
SEM	:	Scanning electron microscopy

TEM	:	Transmission electron microscopy
RBM	:	Radial breathing modes
IM	:	Intermediate modes
TM	:	Tangential modes
SE	:	Secondary electrons
BSE	:	Backscattering electrons
E	:	Energy

LIST OF SYMBOLS

λ	:	Wavelength
μ	:	Micro
θ	:	Theta
e^-	:	Electron
J	:	Joules
nm	:	Nanometer
Y	:	Yttrium
Co	:	Cobalt
Ni	:	Nickel
Fe	:	Iron
Ar	:	Argon
N	:	Nitrogen
C	:	Carbon
$\hat{C}_h$	:	Chiral vector
^oC	:	Degree celsius
μm	:	micrometers

LIST OF TABLES AND FIGURES

CHAPTER ONE

1. INTRODUCTION

1.1. Discovery of carbon nanotubes

Until 1985 the only known crystalline forms of carbon were diamond and graphite. These two materials are completely different in appearance, as well as their mechanical and electrical properties. For example; diamond is an optically transparent material and the hardest material known to man. It is an insulator with high thermal conductivity and with one of the highest electronic band gaps amongst materials [1.1]. Graphite on the other hand is black, soft and conducts electrical current. It can be viewed as a regular stacking of bidimensional hexagonal layers (graphene sheets) of carbon atoms. The graphene sheets are rather widely separated. Their distance is greater than twice the distance between two carbon atoms within the layers (~1.42 Å) [1.2, 1.3]. For diamond; the crystal structure is a face centered cubic (FCC) lattice, each carbon atom is bound to its four nearest neighbours by sp^3 bonds, forming a strong tetrahedral structure (triangular prisms) [1.1]. In graphite, it is well accepted that it has a strong sp^2 covalent bonding joining the carbon atoms in each layer. But there is no agreement regarding the nature of the interlayer bonding. Some authors believe it to be of pure van der Waals type, while others define it cautiously as a much weaker force than the in-plane covalent bond. The van der Waals force between the two graphene sheets arises from the dipole–dipole interaction originating from correlated motion of electrons in the different planes [1.3]. It is the most stable form of solid carbon ever discovered. Figure 1.1 shows the structure of diamond and graphite [1.1].

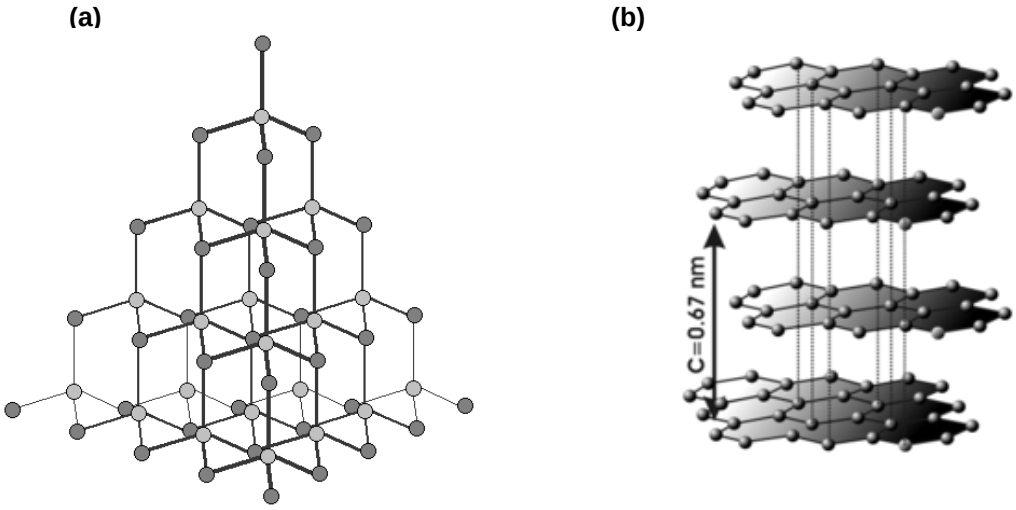

Figure 1.1: (a) Diamond structure showing the carbon-carbon bonding (b) Crystal structure of graphite [1.1].

A new form of carbon, the so called C_{60} molecule was discovered in 1985 by Kroto *et al*. [1.4] while studying small clusters of carbon. They noticed that the fullerene structure which is a hollow spherical molecule with carbon atoms on the surface packed in a structure like a football, i.e. with 12 pentagons and 20 hexagons was highly stable. This molecule became the third crystal structure for carbon and was referred to as the “Bucky Ball”. The molecular structure of a Bucky ball is shown in Figure 1.2.

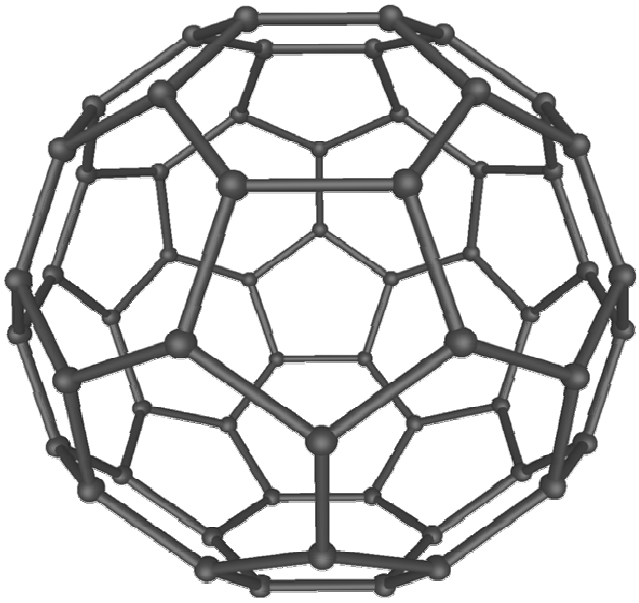

Figure 1.2: Buckminsterfullerene, C_{60}, the third allotrope of Carbon [1.4].

The discovery of thin hollow carbon nanotubes (CNTs) by Iijima *et al*. [1.5] in 1991 by using High Resolution Transmission Electron Microscopy (HRTEM) marked the next important discovery in fullerene science. Since then, carbon nanotubes have been the focus of several researchers. However, the history of CNTs started in the late 1950s with the observation of carbon layered tiny tubes by R. Bacon at Union Carbide and as well as by Radushkevich and Lukyanovich [1.6]. In 1976, Oberlin *et al*. [1.7] reported on the TEM analysis of hollow carbon fibres synthesised by a chemical vapour growth technique. Carbon nanotubes are basically a sheet of graphite folded into a tube of diameter of about 1 nm and length normally of a few micrometers. Structurally, there are two types of CNTs, i.e. single-walled carbon nanotubes (SWCNT) or multi-walled nanotubes (MWNT). Figure 1.3 shows the HRTEM micrographs MWCNTs observed by Iijima et al. [1.5].

Figure 1.3: High resolution TEM image of an individual MWNT (a) d_t = 67 Å and number (N) of walls =5 (b) N=2, d_t = 55 Å (b) N=7, d_t = 65 Å (inner diameter 23 Å) [1.5].

MWCNTs consist of a number of concentric graphite sheets rolled up to form a cylindrical tube of few nm in diameter. Single-walled carbon nanotubes were independently discovered two years later in 1993 by Iijima *et al* [1.8] and

Bethune *et al*. [1.9]. Depending on how the graphite sheet is folded, the carbon nanotube can be either metallic or semi-conducting in nature. A single walled nanotube, for example, can be visualized as a rolled up sheet of graphene. Figure 1.4 illustrates the idea of rolling [1.10, 1.11]. Due to their special structure, perfect carbon nanotubes are light, flexible, thermally stable and chemically inert.

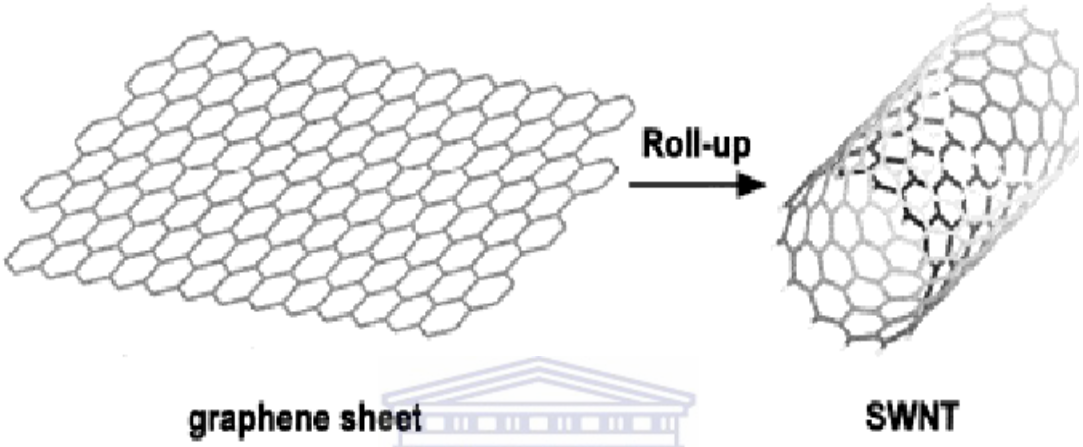

Figure1. 4: A schematic illustration of rolling a graphene sheet [1.10, 1.11].

CNTs can be differentiated into three groups. These are: the zigzag, armchair and chiral nanotubes. The definition of these structures is related to the manner in which they are "rolled up". That is how the two dimensional graphene sheet is rolled up, as in Figure 1.5. If, after rolling, (0,0) and (5,0) overlap each other, then the tube thus formed is called a (5,0) zigzag nanotube. A zigzag nanotube would thus always be parallel to a (n,0) nanotube. An armchair nanotube can be formed by rolling such that (0,0) and (n,n) overlap. The angle between a zigzag and armchair nanotube is always 30º. Any nanotube formed by rolling between these 30º is called a chiral nanotube. This chirality of a nanotube determines its electronic properties. A nanotube is considered to be metallic if (n-m) is a multiple of 3. If it does not satisfy this condition then it is said to be semi-conducting. Thus the angle and the magnitude of the curl, plays a huge role in determining the chirality, and hence the electronic property. Figure 1.6 shows the chiralities of SWCNTs (metallic and semi-conducting) which depend on the chiral vector ($\vec{C}_h$) [1.8, 1.9].

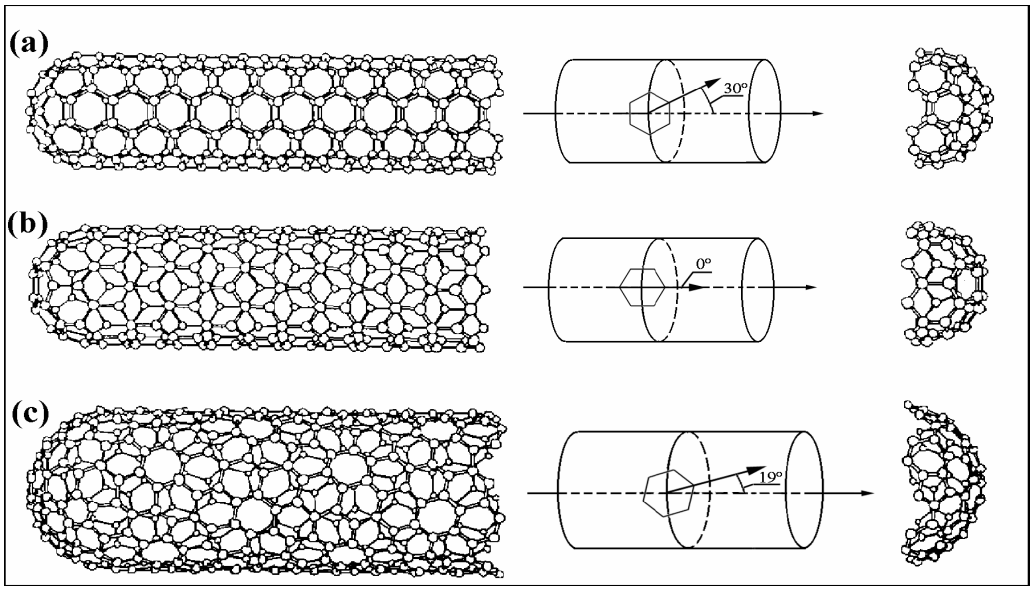

Figure 1.5: Schematic theoretical models of single walled carbon nanotubes, their hexagon orientations and cap structures (a) armchair (5,5) nanotube; (b) zigzag (5,0) nanotube; (c) chiral (10,5) nanotube [1.10, 1.11].

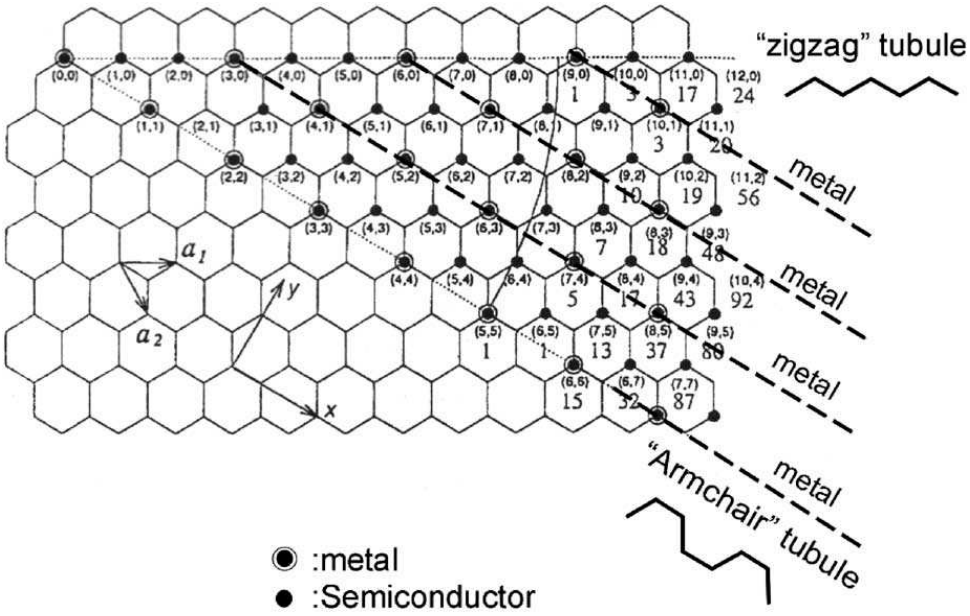

Figure 1.6: The two dimension graphene sheet with given chiralities (n, m). [1.10].

Carbon nanotubes have interesting property; they can be classified as "one-dimensional" molecules [1.12]. This is because they are typically micrometers (μm) in length and 1 nanometer (nm) in diameter. The chiral vector ($\vec{C}_h$) indicated in Figure 1.7, is defined as the line that is connecting two crystallographically equivalent sites of point O and C on a two-dimensional graphene structure. The chiral vector ($\vec{C}_h$) can be defined in terms of the lattice translation indices (n, m) and the basic vectors $\vec{a}_1$ and $\vec{a}_2$ of the hexagonal lattice (a layer of graphene sheet), that is:

$$\vec{C}_h = n\vec{a}_1 + m\vec{a}_2 \tag{1.1}$$

The length of the chiral vector ($\vec{C}_h$) in equation 1.1 is given by:

$$L = \left|\vec{C}_h\right| = \sqrt{\vec{C}_h \bullet \vec{C}_h} = a\sqrt{n^2 + m^2 + nm} \quad = 0.246\sqrt{n^2 + m^2 + nm} \tag{1.2}$$

Since $\left|\overrightarrow{a_1}\right| = \left|\overrightarrow{a_2}\right| = 0.246$ nm. The diameter of the nanotube is given by:

$$d_t = \frac{L}{\pi} = 0.246\frac{\sqrt{n^2 + nm + m^2}}{\pi} \tag{1.3}$$

Using trigonometry the chiral angle θ is defined as:

$$\tan\theta = m\frac{\sqrt{3}}{2n+m} \Rightarrow \theta = \tan^{-1}\left[m\frac{\sqrt{3}}{2n+m}\right] \tag{1.4}$$

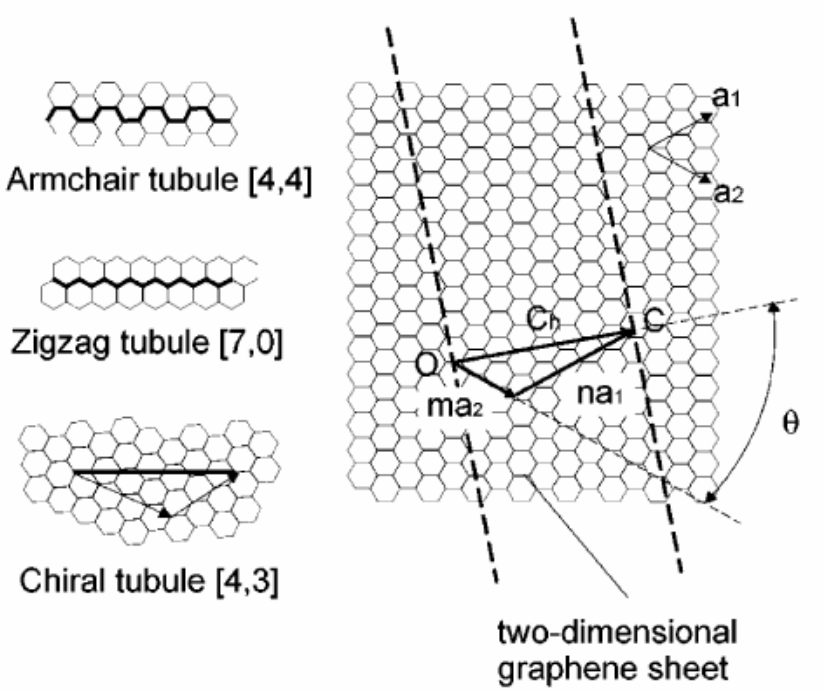

Figure 1.7: The chiral vector $\vec{C}_h = n\vec{a}_1 + m\vec{a}_2$ is defined on the hexagonal lattice of a graphene sheet by unit vectors $\vec{a}_1$ and $\vec{a}_2$ and the chiral angle with respect to the zigzag axis i.e. (n, 0) [1.10].

M. S. Dresselhaus *et al* [1.13] and R. A. Jishi *et al*. [1.14] derived the expression for the length of transitional vector, $\vec{T}$ mathematically. This was derived it in terms of L, the magnitude of $\vec{C}_h$ the highest common divisor of n and m, which is indicated as d_H. If n-m ≠ 3r d_H. Thus the expressions for T result as:

$$T = \left|\vec{T}\right| = \frac{\sqrt{3}L}{d_H} \tag{1.5}$$

And if n-m = 3r d_H. Thus:

$$T = \left|\vec{T}\right| = \frac{\sqrt{3}L}{3d_H} \tag{1.6}$$

They also derived the expression for N, relying on the condition that, each hexagon has two carbon atoms. Hence the number of the carbon atoms unit cell of the tube specified by n and m is 2N, thus the expression for N is given by:

$$N = \frac{2\left(n^2 + nm + m^2\right)}{d_H} \qquad (1.5a)$$

if n-m ≠ 3r d_H, and:

$$N = \frac{2\left(n^2 + nm + m^2\right)}{3d_H} \qquad (1.6a)$$

if n-m =3rd_H:

Therefore, using the above expressions, the diameter and the unit cell parameters of nanotubes can be calculated [1.15].

1.2. Synthesis of carbon nanotubes

There are three main techniques that can be used to synthesize carbon nanotubes: arc discharge, chemical vapour deposition (CVD) and laser ablation.

1.2.1. Arc discharge

During arc-discharge, a high temperature zone between graphite electrodes is needed for the evaporation of carbon atoms to form a high temperature plasma exceeding 3000℃. [1.16]. Two gr aphite rods are used as cathode and anode. The graphite rods are separated from one another by a distance of about 1 mm. A voltage of 20-25 V is applied between the electrodes with the currents between 50 and 120 A. The optimal pressure of helium (He) is mostly kept around 500 Torr. He is used as an inert gas. However, for production of fullerenes, pressure is kept below 100 Torr. For the

synthesis of MWNT, no catalyst is necessary. [1.17-1.19], while for synthesis of isolated SWCNTs, catalysts such as Co, Ni, Fe, Y and Gd are used. But to synthesize bundles of SWCNTs mixed catalysts such as Fe/Ni, Co/Ni and Co/Pt are used. The quality of the nanotubes is very good and they have a high degree of graphitisation. Figure 1.8 shows the schematic of an arc discharge apparatus.

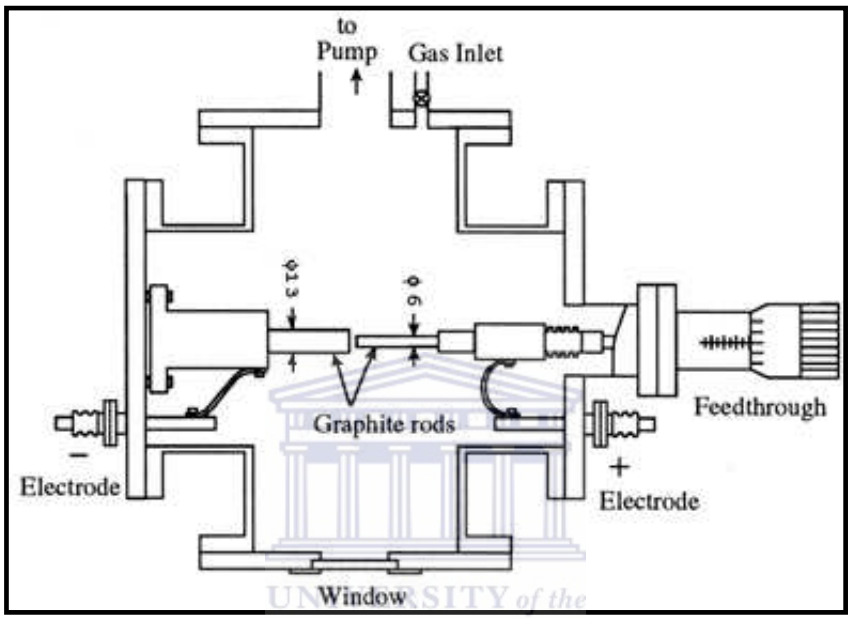

Figure 1.8: Illustration of an arc-discharge apparatus for the production of fullerenes and nanotubes [1.20].

1.2.2. Chemical vapour deposition

During CVD, the layer of metal catalyst particles, which is mostly Nickel (Ni), cobalt (Co), iron (Fe) or combination thereof are deposited onto a suitable substrate such as glass, silicon, aluminium, MgO, etc. The CNTs grown with this technique have their diameters related to the size of the metal particles. There is a two step process to follow to synthesise CNTs using this technique. The catalyst is first prepared by sputtering a transition metal onto the substrate, by using either chemical etching or thermal etching, in order to cause catalyst particle nucleation. Thermal annealing of the coated substrate results in aggregation of the catalyst from which the nanotubes will grow. To

achieve such growth the substrate needs to be subjected to temperatures of between 650-900^{o}C [1.20-1.24]. The yield of CNTs using the CVD process is about 30%. There are several variations or enhancement of the CVD process. These are plasma enhanced CVD (PECVD), thermal chemical CVD, alcohol catalytic CVD, laser assisted CVD, and hot wire or catalytic CVD. Figure 1.9 shows the schematic diagram of Hot Wire (HW) CVD system where a precursor gas usually diluted in hydrogen gas decomposes over a heated filament into reactive radicals and atomic hydrogen. Atomic hydrogen acts as an etching agent to promote the growth of the species. This species grow on a heated substrate that acts as a support.

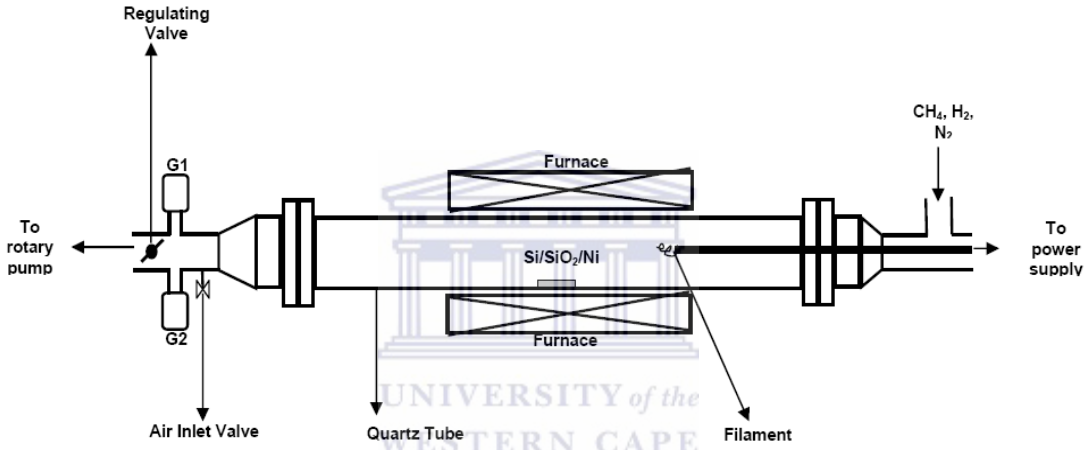

Figure 1.9: Schematic diagram of HWCVD set-up [1.20-1.24].

1.2.3. Laser ablation

In the laser ablation process in order to produce CNTs, a high energy pulsed or continuous laser with high average power is used to vaporize a graphite target located in an enclosed oven. An inert gas such as argon (Ar) is bled into the chamber to push the plume towards the cool Cu collector [1.22, 1.23] as depicted in Figure 1.10. The pressure is kept constant at around 500 Torr. The forward projecting plasma plume is slowed down by the argon gas flow causing the constituents of the plasma to condense and reconstitute as CNTs. These materials are then carried to the back of the furnace by the argon gas flow and the CNTs condense at cooler regions where it is scraped

off for analysis. For SWCNTs catalysts such as Co and Ni are required [1.21]. However if a pure graphite target is used MWNT are produced [1.25]. High yields in the region of 70-90% have been reported. The produced material consists of ropes of SWCNT with a diameter between 10 and 20 nm and up to 100 μm or more in length. The average nanotube diameter and the diameter distribution can be adapted by varying the synthesis temperature and the composition of the catalyst [1.10].

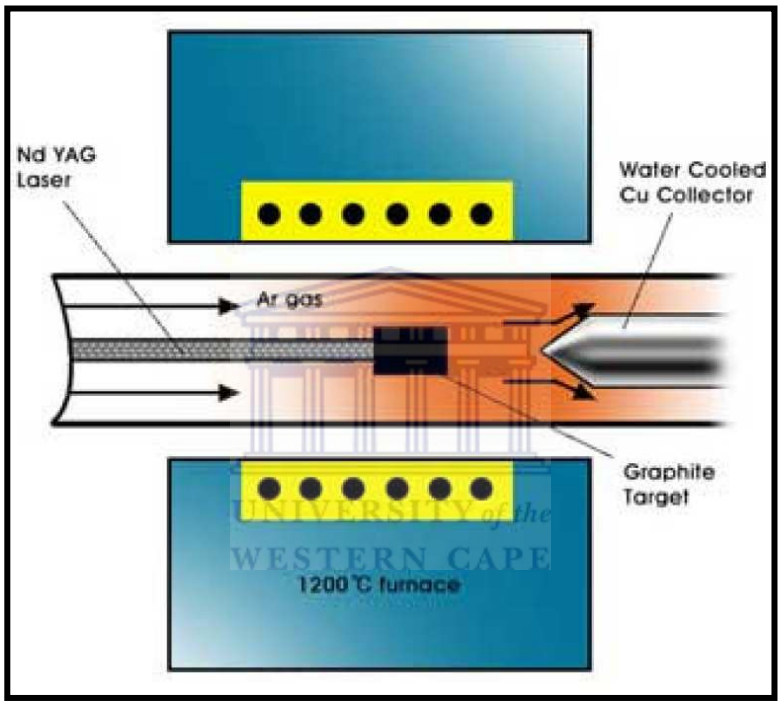

Figure 1.10: Schematic drawing showing the laser ablation process [1.25-1.26].

Puretzky *et al*. [1.27] performed intensified charge coupled detector (ICCD) imaging and the spectroscopy of the Carbon (C) /Nickel (Ni)/Cobalt (Co) plume. This was done at different times after laser vaporization. They found that in each case, the plume exhibits oscillation in both radial and axial directions. It expands radially and axially after ablation, which then compresses the background gas. The interaction between the plume and background gas generates the vortex ring, which efficiently mixes the ablated species with the background gas. Hence, this promotes clustering of the plume species. The motion of the vortex will trap the aggregated nano-

particles in confined volume for a certain time (e.g. roughly 3s within volume of about 1cm^3). After a certain period the plume is pushed by the gas towards the collector with an estimated flow velocity of 0.6 cm/s (0.006 m/s). Then the nanotubes are formed on the cool Cu collector. Figure 1.11 shows the axial focusing of the plume at the different time intervals with $\Delta t \leq 200\mu s$ and different temperatures.

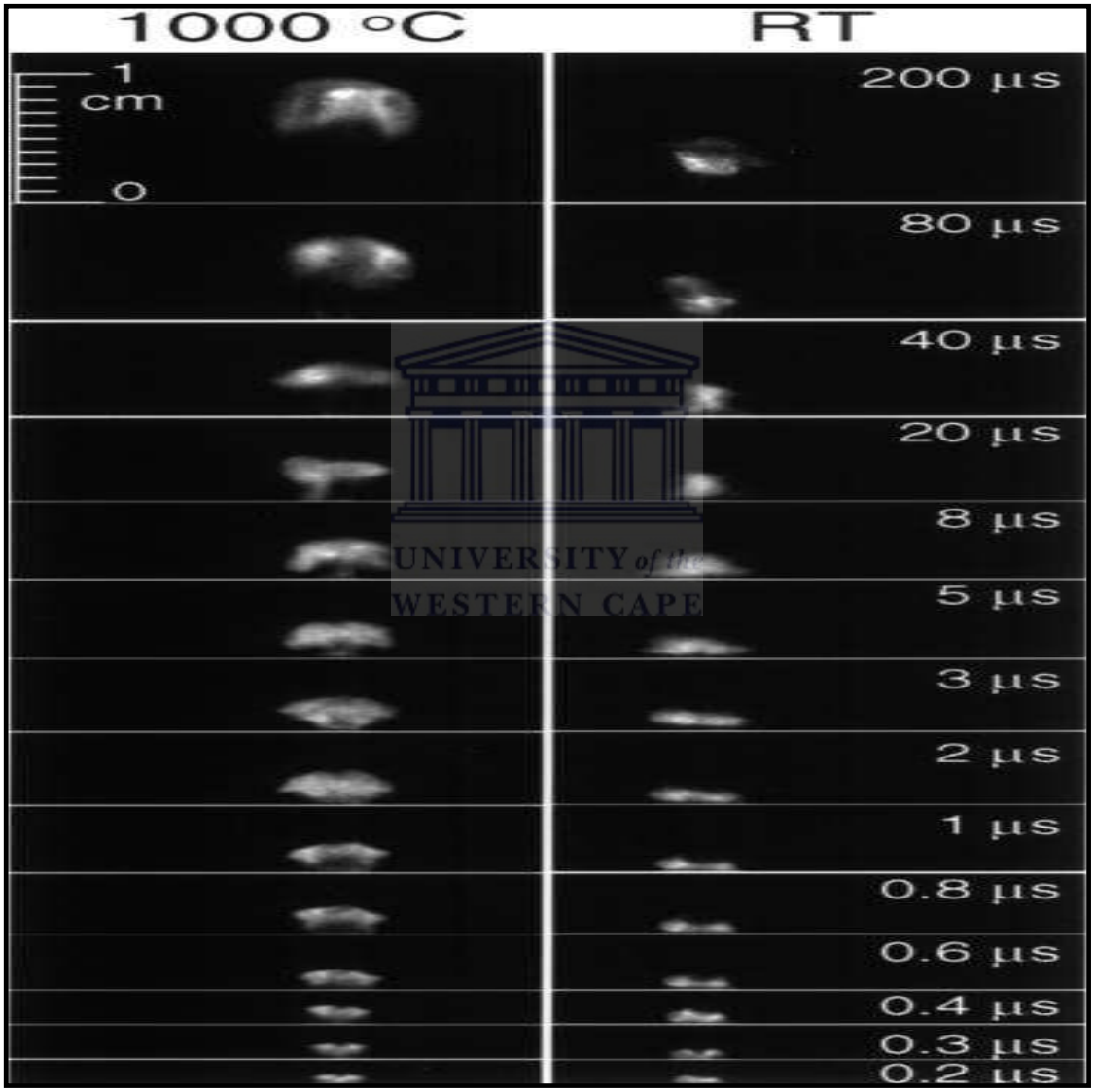

Figure 1.11: Comparison between the propagation of the plume at room temperature and that of 1000 ^{o}C. The plume behaves different at different temperatures and times [1.27].

1.3. Growth mechanism of SWCNTs by laser ablation

In the synthesis of single walled carbon nanotubes, transitional metal catalysts are prerequisite irrespective of the synthesis method used. In the laser ablation process, typical synthesis conditions are 500 Torr of Ar gas at a flow rate of 200 sccm ablating a graphite target with 0.5% each of Ni and Co. A pulsed laser providing an energy density of at least 3 $J.cm^{-2}$ at the target is generally required. Smalley *et al*. [1.28] were the first to report such synthesis conditions.

Scott *et al.* [1.29] speculated that the delay of 50 ns delay between the two pulses enhances the production of CNTs. Because, initially the delay between the two pulses allows incompletely ionized plume to expand enough. This will allow the penetration of the second laser pulse before the target cools. As the vapour caused by irradiated graphite target leaves the surface, small molecular weight carbon species coalesce quickly to form larger molecules and eventually fullerenes and C_{60}. The metal catalyst atoms also coalesce to form clusters at a much lower rate. These metal catalyst particles absorb (and or adsorb) low molecular weight carbon molecules such as C_2, etc. in addition, they may also attach themselves to the fullerenes or graphene sheets to prevent closure. When the metal catalysts remain open at the point of attachment of the particles or atoms of Ni/Co, they grow into nanotubes. This growth occurs from the carbon dissolved in or adsorbed on the catalyst. It can be estimated from calculations of the flux of carbon on catalyst particles at an assumed minimum temperature of 1473 K. At this temperature, a C-atom density of about 10^{18} cm^{-3}, a (10, 10)-carbon nanotube growth will occur at a maximum rate of about 100 μm / μs. Smalley *et al*. [1.28] suggested that at the density of about 10^{21} cm^{-3}, the growth rate of CNTs will be about 100 mm/μs. Puretzky *et al*. [1.27] suggested the growth of CNTs be lasting on the order of a few seconds. According to Scott *et al.*'s assumptions [1.29]; (1) CNTs growth should be limited when the larger diameter metal particles get poisoned or break away from the nanotubes that are forming. This is because the metal particles with larger diameter than nanotubes are seen in the

product. (2) The catalyst particles has to be in the form of liquid in order to efficiently absorb the incoming feed stock and to channel carbon to the growing nanotubes by diffusion. Because of the restrained melting temperature of a very small cluster compared to the bulk material, the particle will remain in the liquid form until it increases in size adequately, then solidify and terminate the growth of the nanotubes.

1.4. Properties of CNTs

Carbon nanotubes (CNTs) have novel properties that provide them with potential usefulness in a broad variety of applications and in different fields (e.g. Material science, Chemistry, nanotechnology and etc.) [1.18].

1.4.1. Mechanical properties

Ever since their introduction into the public domain by Iijima *et al* [1.5] carbon nanotubes (CNTs) have been reported to have high strength and stiffness, because of the carbon-carbon sp^2 bonding [1.30]. CNTs were also noticed to have high Young modulus, which is formulated as:

$$Y = \frac{\text{stress}}{\text{strain}} \qquad (1.7)$$

where the Stress is defined as $\frac{F}{A_0}$ and Strain as $\frac{\Delta l}{l_0}$, F is force applied to any material, A_0 is the cross sectional area through which the force is applied and l_0 is the original length of any isotropic material and Δl is the amount by which the length of the material changes. Treacy *et al* [1.31] measured the amplitude of the intrinsic vibrations of the nanotubes with the aid of a transmission electron microscope (TEM). They reported the elastic modulus of individual MWCNTs, to be about 1.8TPa. This was much higher than that for typical

carbon fibre which was about 680 GPa [1.32]. SWCNTs in comparison have much higher tensile strength and modulus than carbon fibers, and lower density as shown in Table 1.1.

Table 1.1: Mechanical properties of SWCNT and carbon fiber

Properties	**SWCNT** [1.33]	**Carbon Fiber** [1.34]
Tensile Strength (GPa)	~37	~4
Tensile Modulus (GPa)	~640	~400
Elongation at break (%)	~5.8	~2.0
Density (g/cm^3)	~1.3	~1.75

1.4.2. Electrical properties

There has been a considerable practical interest on the conductivity of carbon nanotubes. CNTs having their structural parameters (n, m) that show how much the nanotube can be twisted can be highly conducting if (n-m) is a multiple of 3. In this case they are considered to be metallic. This conductivity depends on their chirality and also on their diameter. In both types of tubes viz. MWNTS and SWCNTs, the conductivity is different. In MWNTs the conductivity is unstable since armchair type structures appear to conduct better than for metallic types. Within the MWNTs, the current over individual tubes was found to be distributed non-uniformly. In the case of SWCNTs, the current across the different parts of metallic SWCNTs does not change. This is probably due to the fact that the SWCNTs are one-dimensional (1D) structure, while the MWNTs are considered to be 2D, due to their large diameters. In semi-conducting SWCNTs, the transport of current changes abruptly at different positions along the tubes [1.35].

1.5. Potential applications of carbon nanotubes

The extraordinary properties of CNTs and their potential applications in advanced electronic devices make them an important strategic material for research. There are many possible applications of carbon nanotubes both on the nanometre scale and in the macroscopic range that attract the attention of scientists and engineers. Some applications have been proved on the laboratory scale such as field-effect transistors [1.36], torsional nanosprings [1.37, 1.38] or as single vibrating strings for ultra small force sensing devices. Nevertheless, there is a major difficulty in building these devices on a large scale. This is mainly because of the poor control of the tubes that are synthesized in current synthesis methods. Presently, the control of the chirality i.e. the control of the electronic properties limits the scaling up of this material for electronic applications. So far, CNTs have been applied in applications such as nanocomposites where their high strength is used to improve mechanical strength of mouldings for use in the motor industry. When the exact control of the chirality will be achieved, this will be a major breakthrough in material science.

1.6. Aims and outline

Despite the considerable experimental and theoretical work that is associated with carbon nanotube research, the exact growth mechanism of these materials has not been realized. Laser spectroscopy of plasma plumes affords the researcher opportunities of studying the growth process in its early stages. In this study, the optical emission features of the laser ablated carbon plume that is generated in argon gas are investigated. The optical emission spectra are studied by varying different experimental parameters such as gas pressure and flow rate. In general, the aim of this study is to investigate the changes of electron temperature and density when gas flow and pressure are varied. The effects of the flow rate and argon pressure on the synthesis of carbon nanotubes is also corroborated by Raman spectroscopy and scanning electron imagery of material prepared at the exact experimental conditions under which optical emission studies were made, these conditions are explained in details in chapter three.

The outline of this thesis is laid out as follows:

Chapter one focuses on the introduction of carbon allotropes such as diamond, graphite and carbon nanotubes. Here, a brief overview on the discovery of carbon nanotubes was given and the properties, applications and synthesis of carbon nanotubes were covered.

Chapter two focuses on the optical emission spectroscopy of graphite composite targets containing transitional metals. It also gives a brief description on the theory of electron temperature and density measurements and how these data can be deduced from optical emission spectra.

In chapter three, details of the experimental setup, the optical emission studies and the conditions under which carbon nanotubes were synthesized are presented. Raman spectroscopy which is a primary technique in the

characterization of carbon nanotubes is discussed. Scanning electron microscope (SEM) which was also used in this study is described.

Chapter four reports on the results and discussions of OES, Raman and SEM work. A discussion of these results is also presented.

Chapter gives a summary of the work presented in this thesis.

1.7. References

[1.1] Kittel. C., *Introduction to Solid State Physics* (John Wiley & Sons, Inc., New York, N.Y.) 1966; Ashchroftn. W. and Mermin. N. D., *Solid State Physics* (HRW International Editions, Philadelphia) (1976); Dresselhaus. M.S, Dresselhaus. G., Sugiharka, Spaini. L. and Holdberhg. *Mater. Sci.* Vol. **5** (1988).

[1.2] J. D. Bernal., Proc R. Soc London, Ser. A **106** (1924)

[1.3] J. C. Charlier, X. Gonze and J. P. Michenaud, Europhys. Lett, **28** (6) 403 (1994)

[1.4] H. W Kroto, J. R Heath, S. C. O'Brien, R. F Curl, R. E Smalley, *Nature* Vol. **318** 162 (1985).

[1.5] Sumio Iijima, Helical microtubules of graphite carbon, *Nature* **354** 56 (1991)

[1.6] Bacon R, Bowman JC. Production and properties of graphite whiskers. *Bull Am Phys. Soc*. **2** 131 (1957).

[1.7] A. Oberlin, M. Endo & T. Koyama*, journal of crystal growth* **32** 335 (1976).

[1.8] Sumio Iijima, T. Ichihashi, Nature **363** 603 (1993).

[1.9] D.S Bethune, C. H Kiang, M. S. de Vries, G. Gorman, R. Savoy, J Vazquez, R. Beyers, *Nature* **363** 605 (1993).

[1.10] R. Saito, G. Dresselhaus, and M. S. Dresselhaus, *Properties of Carbon Nanotubes.* Imperial Collage Press; Singapore, (1998).

[1.11] Odom, T.W., J.L. Huang, P. Kim, and C.M. Lieber, *Phys. Chem*. B **104** 2794 (2000).

[1.12] S. Roth and C. Carroll. *One Dimensional Metals*. WILEY-VCH, 2004.

[1.13] M. S. Dresselhaus, G. Dresselhaus and P. C. Eklund, '*Science of Fullerenes and carbon nanotubes*', Academic Press, San Diego, (1996).

[1.14] R. A. Jishi, M. S. Dresselhaus and G. Dresselhaus, *Phys. Rev. Lett.* B, **47** 16 671 (1993).

[1.15] P. J. F. Harris, '*Carbon Nanotubes and Related Structures*: New Material for the 21st Century ', Cambridge University Press, Cambridge, **69**, 83 (1999).

[1.16] C. Journet, W.K. Maser, P. Bernier, A. Loiseau, M. Lamy de la Chapelle, S. Lefrant, P. Deniard, R. Lee, J.E. Fischer, *Nature* **388**, 756 (1997).

[1.17] P.A. Ajayan, S. Iijima, Nature **358**, 23 (1992).

[1.18] V.P. Dravid, X. Lin, Y. Wang, X.K. Wang, A. Yee, J.B. Ketterson, R.P.H. Chang, *Scie.* **259**, 1601 (1993).

[1.19] S. Iijima, Mater, Sci. Eng. B **19**, 172 (1993).

[1.20] Y. Saito, M. Inagaki, Jpn. J. *Appl. Phys*. **32**, 954 (1993).

[1.21] Ren, Z. F., Huang, Z. P., Xu, J. W., Wang, J. H., Bush, P., Siegel, M. P., and Provencio, P. N. **282** (5391) 1105 (1998).

[1.22] Ren, Z. F., Huang, Z. P., Wang, D. Z., Wen, J. G., Xu, J. W., Wang, J. H., Calvet, L. E., Chen, J., Klemic, J. F., and Reed, M. A. *Applied Phys. Lett.* **75** (8) 1086. (1999).

[1.23] Yudasaka, Masako, Kikuchi, Rie, Matsui, Takeo, Ohki, Yoshimasa, Yoshimura, Susumu, and Ota, Etsuro, *Applied Phys. Lett.* **67**(17) 2477 (1995).

[1.24] Yudasaka, Masako, Kikuchi, Rie, Ohki, Yoshimasa, Ota, Etsuro, and Yoshimura, Susumu, *Phys. Lett.* **70** (14), 1817 (1997)

[1.25] T. Guo, P. Nikolaev, A.G. Rinzler, D. Tomanek, D.T. Colbert, R.E. Smalley, J. *Phys. Chem*. **99** 10694 (1995).

[1.26] A. Thess, R. Lee, P. Nikolaev, H. Dai, P. Petit, J. Robert, C. Xu, Y.H. Lee, S.G. Kim, A.G. Rinzler, D.T. Colbert, G.E. Scuseria, D. Tomanek, J.E. Fischer, R.E. Smalley, *Science* **273** 483 (1996).

[1.27] A. A. Puretzky, D. B. Geohegan, X. Fan, S. J. Pennycook, *Appl. Phys*. A **70** 153 (2000).

[1.28] R.E. Smalley: *Acc. Chem. Res*. **25**, 98 (1992)

[1.29] C.D. Scott, S. Arepalli, P. Nikolaev, and R. E. Smalley: *Appl. Phys.* A **72** 573 (2001)

[1.30] D. H. Robertson, D. W. Brenner, J. W. Mintmire, *Phys*. *Rev*. B **45** 12592 (1992).

[1.31] M. M. J. Treacy, T. W. Ebbesen, and J.M. Gilson, *Nature* **381** 678 (1996).

[1.32] R. L. Jacobsen, T. M. Tritt, J. R. Guth, A. C. Ehrlich, D. J. Gillespie, *Carbon* **33** 1277 (1995).

[1.33] H. R. Baughman, *Science*, **297** 787 (2002).

[1.34] Sander J. Tans, Alwin R. M. Verschueren, Cees Dekker, *Nature* **393** 49 (1998).

[1.35] B. Q. Wei, *Appl. phys Lett.* **79** 1172 (2001).

[1.36]. P. Avouri, *Acc. Chem. Res*. **35** 1026 (2002).

[1.37] P. A. Williams, S. J. Papadakis, A. M. Patel, M. R. Falvo, S. Washburn, and R. Superfine, *Appl. Phys. Lett*. **82** 805 (2003).

[1.38]. A. M. Fennimore, T. D. Yuzvinsky, W.-Q. Han, M. S. Fuhrer, J. Cumings, A. Zettl, *Nature* **424** 408 (2003).

CHAPTER TWO

2. OPTICAL EMISSION SPECTROSCOPY OF GRAPHITE AND GRAPHITE COMPOSITE TARGETS

2.1. Introduction

Optical emission spectroscopy (OES) is a technique that is principally utilised to investigate atoms, ions and molecules within the plasma, the fourth state of matter. It is also widely used to investigate laser generated plasma plumes. When atoms, radicals or molecules are excited to higher energy levels they relax to lower levels by emitting radiation. Analysis of this radiation provides information about emitting species properties, densities, electron temperatures, atom, atom-atom and ion-atom collisional effects, energy distribution of species, charge transfer between plasma constituents, and electric and magnetic fields. Since a complete description of phenomena taking place within the plasma is very complex, the use of OES as a diagnostic tool for emitting species appears to be a promising tool for understanding the plasma processes. Furthermore, since the analysis of OES observations is dependent on the source of emission and the understanding of the physical processes occurring within the source, certain criteria has to be taken into account to interpret these observations. For instance, to deduce the electron temperature from Boltzmann or Saha equations, local thermodynamic equilibrium (LTE) has to be considered. The use of OES in the analysis of low density, low temperature plasmas have yielded great information about the properties of materials within the plasma [2.1- 2.3].

2.2. Carbon emission systems detected in graphite

Radhakrishnan *et al.* [2.4] studied the ablation of pure graphite target in a high vacuum (10^{-8} Torr) at room temperature. Argon (Ar) and oxygen (0_2) gases were flowing at a constant pressure of 2 Torr. Under these conditions, the characteristic Swan band emissions from the C_2 molecule were detected with band heads at 463.5 nm ($\Delta v = 1$), 516.5 nm ($\Delta v = 0$), and 550.5 nm ($\Delta v = -1$), respectively, where Δv is the vibrational sequence. In both Ar and 0_2, the Swan bands were intense and could be detected up to 40 microseconds (μs) when using a 1 μs gate step. The ablated material was analysed by transmission electron microscopy (TEM) where amorphous carbon was observed. Aquaviva *et al* [2.5] studied the role of gas phase reactions in the expansion process of the plasma produced by excimer laser (308 nm) during graphite ablation in nitrogen. The pressure used ranged from 0 to 400 mTorr and the optical emission spectra were acquired at different time delays, up to ~3 μs from when the laser pulse first interacted with the target. At short distances of less than 1 mm from the target surface, the atomic carbon lines at 193.09 nm, 247.86 nm, 394.22 nm and 396.14 nm and the bands of C_2 Deslandres D' Azambuja system were detected. The CII emission lines were also observed. At high distances greater than 1 mm from the target surface, the carbon nitride (CN_x) and C_2 Swan bands were the predominant emitting species. Figure 2.1 shows the typical emission spectra detected at different distances.

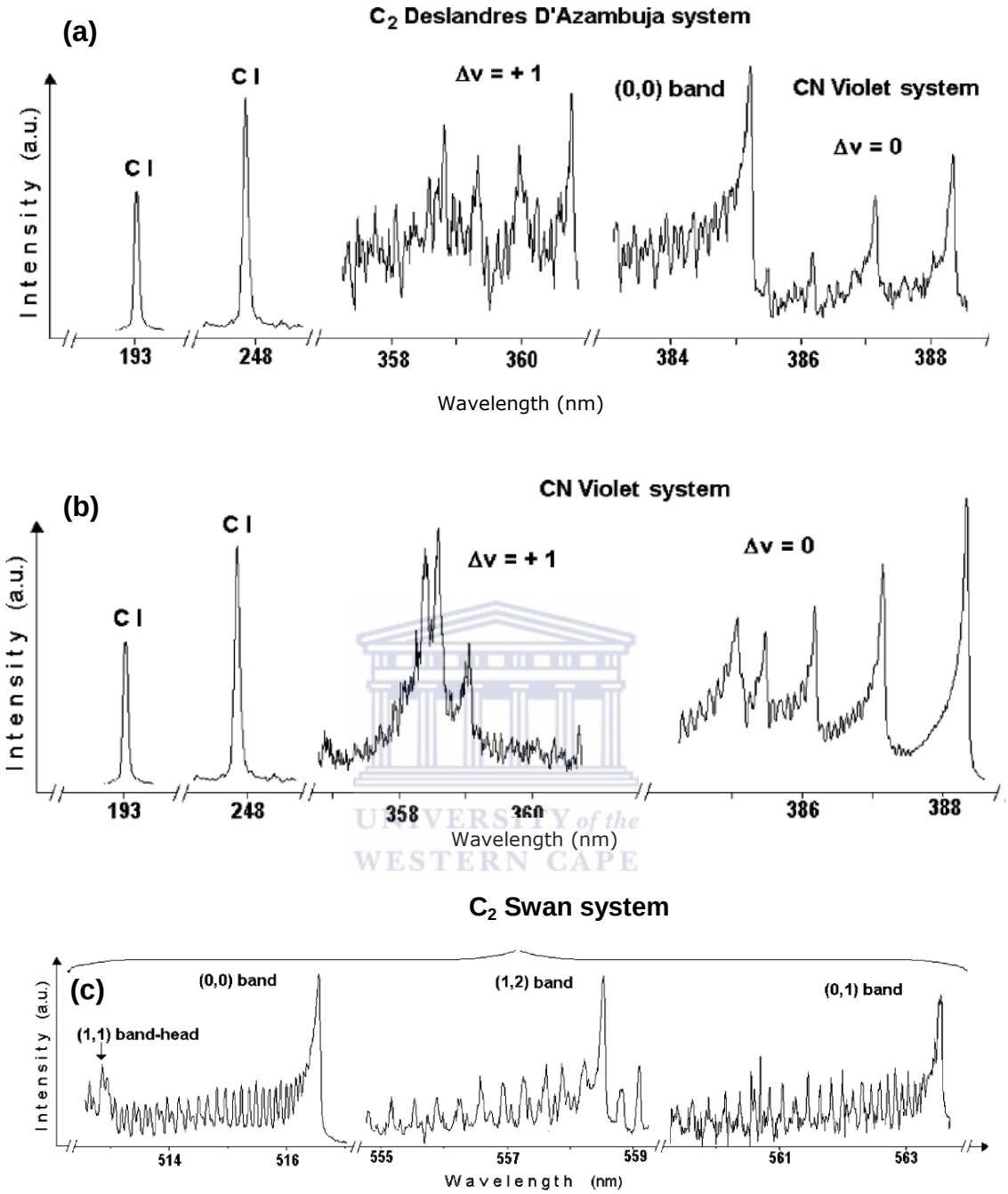

Figure 2.1: Typical emission spectra detected at shorter distances and larger distances: (a) C_2 Deslandres system detected at shorter distances, (b) CN violet system detected at longer distances, and (c) C_2 Swan band system [2.5].

Acquaviva *et al* [2.5] suggested that CN_x formation was due to the gas-phase reactions between the carbon species in plume and the surrounding N_2 gas. Hence, the precursor was found to be the atomic carbon since, in the considered nitrogen gas (N_2) pressure range, the intensity C(I) emissions at the wavelengths of 193.09 nm and 247.86 nm decreased with the increase of CN intensity. The emission of C_2 molecules were enhanced by the N_2 because in the region where the CN intensity dropped, the C_2 emissions increased. Voevodin *et al.* [2.6] also studied the fullerene like-CN_x, and found that the CN radicals form in the reactions with the background gas. Moreover, the pressure at which CN emission intensity was maximized was found to be significantly dependent on the location of the sampling region. This was confirmed by imaging the plume at different background pressures. At a relatively low pressure of 5 mTorr N_2, they also noticed an intensification of the emission near the substrate; it corresponds to plume excitation by collision. That is with either the substrate surface or with species rebounding from the substrate surface. In addition, when the pressure was increased above 15 mTorr, a plasma “bubble” formed. At 30 mTorr, plasma “bubble” development near the substrate surface excitation was especially clear in photographs from CN radicals. At the higher pressure, above 75 mTorr, the collisional deceleration was found to be causing the plume to terminate at about 2 cm away from the substrate.

Dinescu *et al*. [2.7] studied the effects of parameters such as laser energy density, gas pressure, and distance from the target on CN and C_2 formation. At a pressure of 100 Pa and energy density of 10 $J.cm^{-2}$, they found that as the distance from the target increased, the C_2 emission intensity exhibited a rapid decrease and had a narrow profile that reached its maximum near the target. While the CN radical had a larger profile that reaches a maximum at larger distances of about 6 mm from the target as shown in Figure 2.2 (a). CN and C_2 were also noticed to be depending on the laser energy density as shown in Figure 2.2(b). CN radical emission was identified to be increasing for distances larger than 2 mm. However, at shorter distances of less than 2 mm, it was difficult to conclude on the dependence of CN emission on energy density.

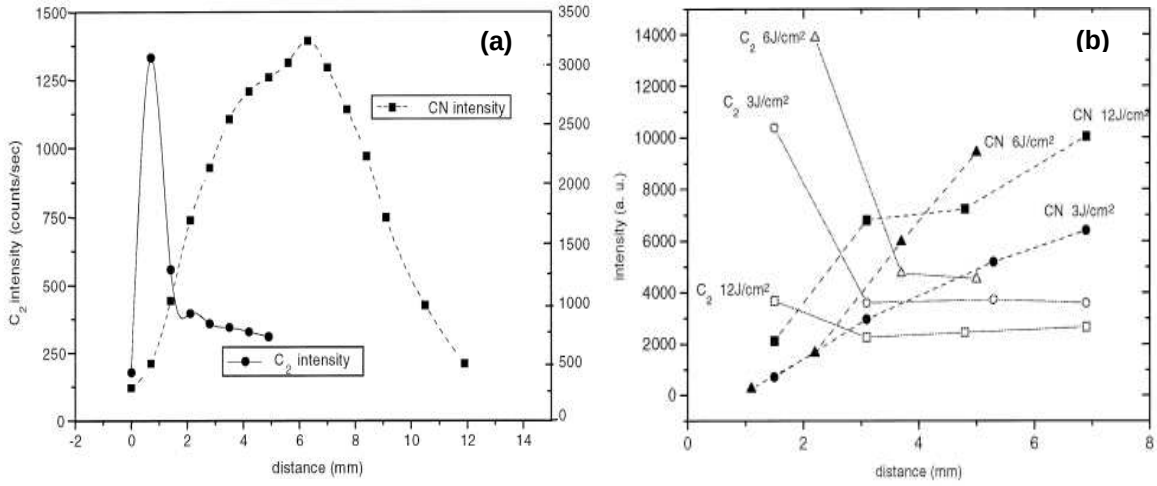

Figure 2.2: (a) Behaviour of CN and C_2 bands intensities along the plasma axis. (b) Dependence of CN and C_2 systems on the distance at energy densities of 3, 6, 12 Jcm^{-2} and at N_2 pressure of 50 Pa [2.7].

2.3. Notations used for classifying spectral carbon systems in OES

In quantum mechanics point of view, Deslandres D' Azambuja (DDA) electronic transition involves states of singlet spin multiplicity because its multiplicity is defined by n+1 or 2S+1 which is equals to one, when its total spin quantum number S = 0 or its unpaired electron n is zero. The DDA system has its electronic transition between $C^1\Pi_g$ and $A^1\Pi_\mu$. The C_2 DDA band ($C^1\Pi_g$- Π_μ) is found in the wavelength range of 285-1000 nm [2.8]. The Swan bands system is between the triplets' states and its transitions is given as $d^3\Pi_g$ - $a^3\Pi_\mu$. This is because its multiplicity is 3, when S = 1 or when n = 2. The C_2 Swan bands ($d^3\Pi_g$- $a^3\Pi_\mu$) as shown in Figure 2.3 are the most prominent bands found in the visible region of between ~400 - 666 nm. They are easily excited in flames or in arc discharges through gases containing carbon. The emission spectrum of CN is dominated by the violet system. The violet system of CN is due to the electronic transition between the $B^2\Sigma^+$ and $X^2\Sigma^+$ molecular states and has doublet states. This is because it has a spin multiplicity of 2 or has one unpaired electron, due to its total spin quantum

number which is ½ [2.9]. The total spin quantum number is zero if and only if the sub-shell is completely filled where the total orbital angular momentum quantum number L is equals to the total spin quantum number S, for instance helium (He) ground state ($1s^2$), Neon, Ne ($1s^2$, $2s^2$, $2p^6$), etc, has L = S = 0 because they have a complete filled sub-shell.[2.9].

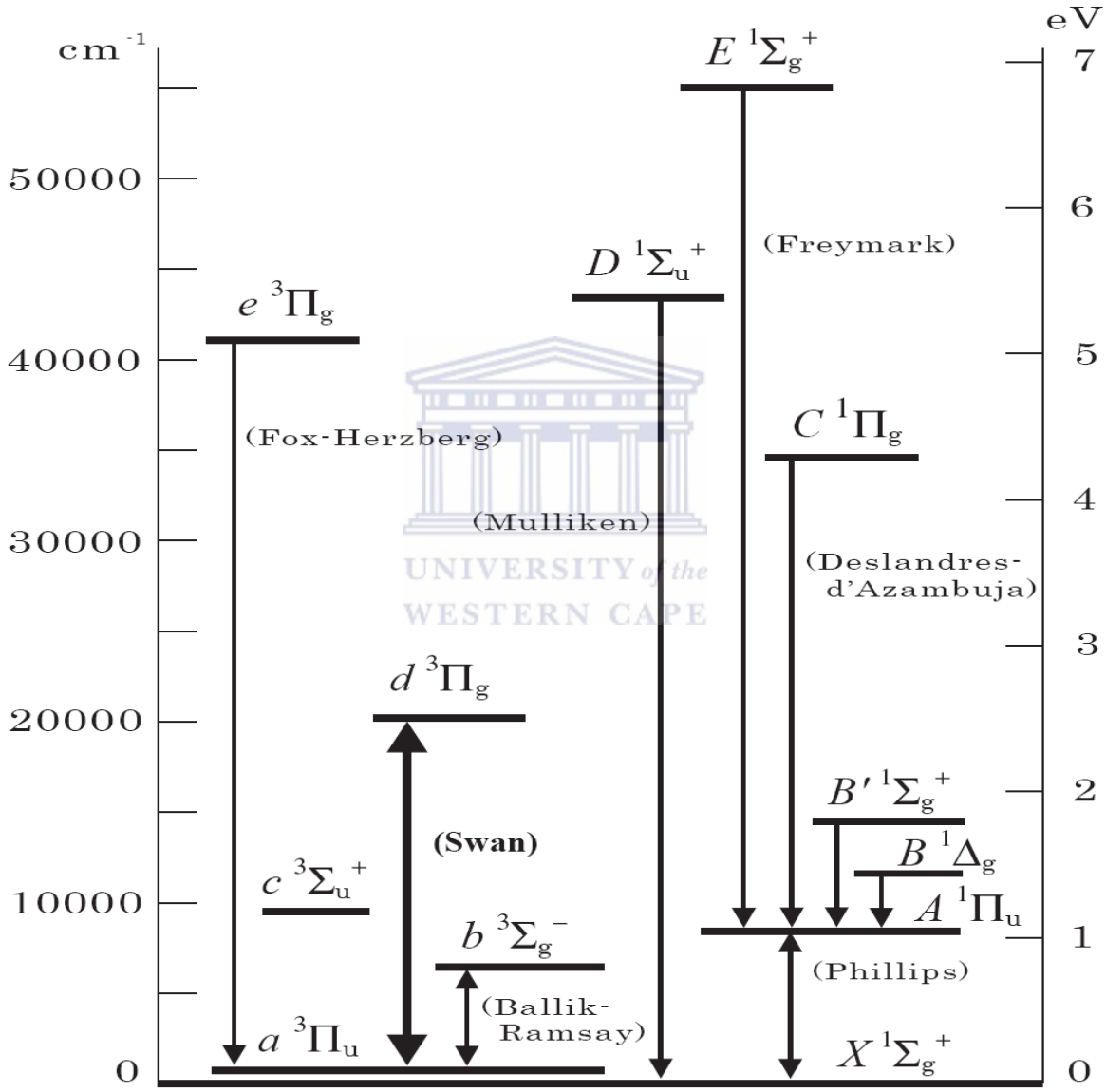

Figure 2.3: The low-lying electronic states of C_2. The directions of the arrows indicate the C_2 emissions and absorption in different energy levels [2.8].

2.4. Graphite mixed with transitional metal catalyst(s)

It was reported earlier that the ablation of graphite mixed with metal catalyst (graphite composite) in a high temperature furnace in the presence of Ar gas flow of 200 sccm, resulted in the synthesis of single wall carbon nanotubes. Small carbon fragment molecules such as C_2 Swan and Deslandres systems and C_3 have been observed in emission during the laser synthesis of SWCNTs. It was speculated that they play a key role as carbon feed stock during the nanotubes growth. In general, several parameters were reported to contribute to the growth of SWCNTs, e.g. the laser wavelength, pressure, target composition, etc [2.10].

- The use of a laser operating at 1064 nm was reported to result in a production of large quantities of SWCNTs when compared to a laser operating at 532 nm. This can be attributed to higher pulse energy per shot or higher average power at the target surface resulting in a higher rate of vaporization of target material. Optimum results in terms of production rate and the purity of SWCNTs were obtained with the use of continuous-wave (cw) Nd: YAG laser operating at 1064 nm. A production rate exceeding 250 mg/h with maximum synthesis rate of 450 mg/h was achieved [2.11].

- Smalley *et al.* [2.12] reported the synthesis of SWCNT using lasers in an ambient argon gas flowing at a pressure of between 400-500 Torr inside 25 mm inner quartz tube in furnace operating at 1200 ^{0}C. The material produced was of high quality. However, Tomoaki *et al*. [2.13] reported that nitrogen gas (N_2) flowing at the pressure of about 600 Torr yielded larger amount SWCNTs than Ar gas flowing at the same pressure. They attributed this to the obtained optical emission spectroscopy results, where the N_2 having a higher initial temperature decreased faster than in the case of Ar gas. Furthermore, since

the N_2 molecules are lighter in mass, the C_2 molecules excited by the laser lose less energy by collision as shown in Figure 2.4. In Ar gas, the C_2 molecules at earlier stage loose more energy due to its higher mass. Tomoaki *et al*. also noticed that N_2 enhances the C_2 emission and decreases the vibrational temperature of C_2 molecules after ablation, during the formation of CNTs.

- Maser *et al.* [2.14] heated a graphite rod containing Ni/Y and Ni/Co catalysts in an argon atmosphere with a cw-CO_2 laser. They found that Ni/Y (4.2/1 at. %) yielded the most nanotubes, followed by the Ni/Y (2/0.5 at. %) mixture, then Ni/Co (2/2 at. %).

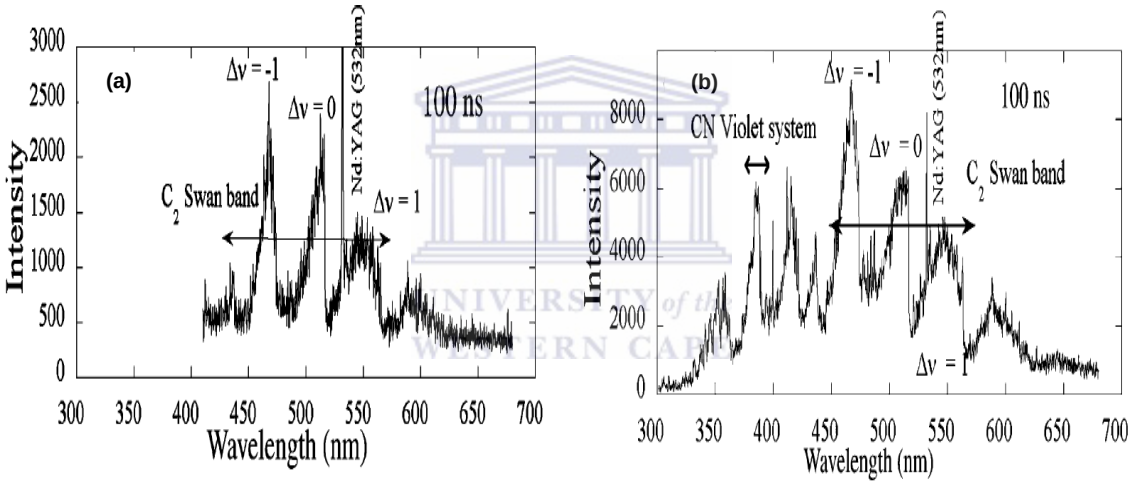

Figure 2.4: Emission spectra measured at the same delay times after laser ablation: (a) 100ns in an argon ambient gas, (b) 100ns in nitrogen ambient gas [2.13].

2.5. Influence of laser parameters

In most cases, the laser wavelength has a major effect on the yield of the ablated materials. Lasers with short wavelength in the ultra violet region of high photon energy are mostly used. This is because, at shorter wavelengths, reflectivity of the laser at the target surface for most materials is lower than at long infrared wavelengths. Reduced reflectivity implies that more laser energy

is imparted to the target which in turn increases the number of ablated particles. In the UV region, the absorption coefficient is larger so that the beam energy is absorbed in thin surface layers. Hence, this makes the ablation to occur more efficiently. Abdellatif *et al.* [2.15] also reported the influence of laser wavelength on the electron density and plume temperature, where the Nd: YAG laser of 1064, 532 and 355 nm was applied and found that the laser irradiance required for plasma formation appeared to be much more higher for the 1064 nm than for 532 and 355 nm wavelength. Günther *et al* [2.16] used Nd: YAG and Excimer laser operating at the wavelengths of 266, 213 and 193 nm to study the effect of the wavelength on the particle size distribution. They observed that shorter wavelengths give rise to smaller particles. This was attributed to a lower penetration depth inside the target. Bogaerts *et al* [2.17] studied the effect of laser irradiance on copper (Cu) using Nd: YAG laser (266 nm, laser pulse of 5 ns) and found that as the laser irradiance increases the surface temperature, melt depth evaporation rate and evaporation depth increase as shown in Figure 2.5.

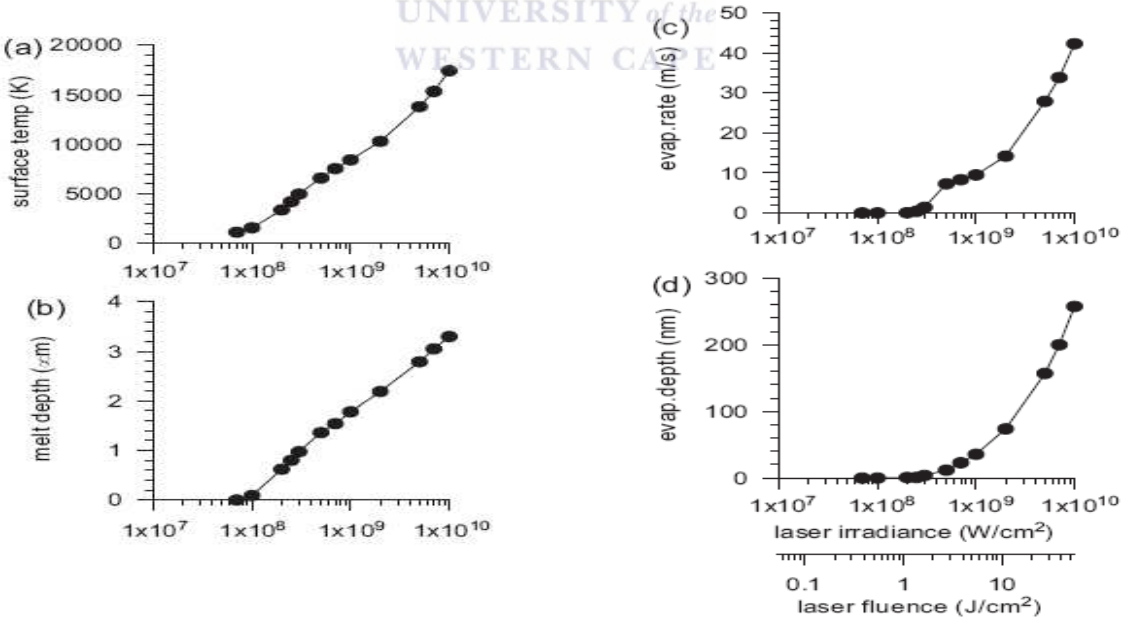

Figure 2.5: (a) Maximum surface temperature, (b) Maximum melt depth, (c) Maximum evaporation rate and (d) Total evaporation depth, as a function of laser irradiance [2.17].

Wolfgang *et al.* [2.18] identified that when the Nd: YAG laser was used, the fourth harmonic of 266 nm removed more material on the copper sample than when the fundamental wavelength 1064 nm was used. Dam *et al*. [2.19] reported that the energy density of the laser pulse has to be greater than a certain threshold value of the target material, so that all the carbon species can be removed stoichiometrically from the target. However, if the energy density is extremely high, it may result in the injection of large target fragments, which will increase the number of droplets on the film substrate.

2.6. A brief description of the plasma plume

The plume produced in the laser ablation process is ionized and it includes atoms, ions, electrons, atomic clusters, etc. When the plume is in the sample plane as the incident laser beam; the laser energy is continuously absorbed by the plasma during the lifetime of the plume. In this way, the particles in the plasma gain kinetic energy and their temperature and degree of ionization increases. The ionized plasma is mostly formed at few micrometers in the vicinity of the target surface. As the plume expands away from the target with a strong forward-directed supersonic velocity distribution, the visible light observed from the plume, due to fluorescence and recombination processes occurring in the plasma is observed. This occurs when the excited electrons fall back to the lower energy level as the atom cools, spontaneously emitting the photons. The intensity of the light emitted, I_{em}, is defined by Maxwell-Boltzmann equation:

$$I_{em} = A_{ji} h v_{ji} \left[\frac{N g_i}{g_0} \exp\left(- \frac{\Delta E_{ij}}{K_B T}\right) \right] \qquad (2.1)$$

where h is defined as Planck constant, k_B as Boltzmann constant, v_{ji} is the frequency of transition, A_{ji} is Einstein's transition probability for the given electronic transition and g_i and g_0 are the respective statistical weights for

upper state *j* and lower state *i* of the electron bands, ΔE_{ji} is the energy difference in joules between *j* and *i* states, respectively. This emission of radiation is then collected through the focusing optics and carried by an optical fibre to the intensified charge coupled detector (ICCD) attached to the spectrograph. The spectrograph measures the intensity versus the wavelength of the radiated light. This is a sophisticated way that has been employed to investigate the role of plasma generated by laser induced breakdown spectroscopy (LIBS), also called laser induced plasma spectroscopy (LIPS), as the source of emission spectrum for analytical purposes [2.1, 2.20].

2.6.1. Electron temperature measurements

There are several methods that can be used to calculate the electron temperature. The most widely used methods are Boltzmann's law and the Saha-Boltzmann's law. The Boltzmann's distribution in equation 2.1 can only be used by assuming that the plasma is in local thermodynamic equilibrium (LTE). Then this will be used to estimate the population of the excited state. This method uses several emission lines from single species such as C, Fe, Ni, and etc, to obtain the electron temperature, provided there is sufficient difference in energy between their upper levels. Moreover, if more emission lines are employed, the Boltzmann plot will provide a more accurate estimate of electron temperature. Hence, a linear fit to experimental data not only validates the assumption of the Maxwell electron distribution, but serves also as a procedure to check for errors in line assignments or transition probability values [2.20]. Saha-Boltzmann's distribution is another possible method that is used to obtain the electron temperature. This method combines the number densities of consecutive ionization stages of a gas in a Maxwell-Boltzmann factor, resulting in the population distribution for each constituent species. The Saha equation is shown in equation 2.2 and it depends strongly on LTE:

$$\frac{I'}{I} = \left(\frac{f^{i}g\ \lambda^{3}}{fg\lambda'^{3}}\right)\left(4\pi^{3/2}a_0{}^{3}n_e\right)^{-1}\left(\frac{kT_e}{E_H}\right)\times\exp\left(\frac{E' + E_\infty - E - \Delta E_\infty}{kT}\right) \quad (2.2)$$

where the primed symbols represent the line of an atom with higher ionization stage, f is the oscillator strength, g is the statistical weight, a_o is the Bohr radius, E_H is the ionization energy of the hydrogen atom, E is the excitation energy, and ΔE_∞ is the correction to the ionization energy E_∞ of the lower ionization stage due to plasma interactions [2.20], and it is given by [2.12, 2.13]:

$$\Delta E_\infty = 3z\frac{e^2}{4\pi\varepsilon_0}\left(\frac{4\pi n_e}{3}\right)^{1/3} \quad (2.3)$$

where z= 2 for the lowest ionization state.

2.6.2. Electron density measurements

The shape and the width of the spectral lines emitted by plasma are dependent on the collisional processes between the atoms and ions. The main mechanisms that contribute to the broadening of the spectral lines are: Stark, resonance, Doppler and instrumental broadenings. The effect of resonance broadening is proportional to the ground state number density and the transition oscillator strength. Doppler broadening is the main contributions to the spectral lines for ablation in vacuum, where the ablated species show high expansion velocities. This is due to the Doppler shifts experienced by the various species in the plume exhibiting different velocities components in the direction of the observer. This is defined as:

$$\Delta\lambda_D = \frac{\lambda_{rest} v_{radial}}{c} \tag{2.4}$$

where λ_{rest} is the wavelength that one would measure if the object was at rest and V_{radial} is the speed along the line of sight. Instrumental broadening is neglected as this is minimised by setting the spectrograph at its maximum resolution. The Stark broadening of spectral lines in plasmas are caused by collisions of charged species, resulting in both a broadening of the line and a shift in the peak wavelength. Equation 2.5 defines the full width half maximum (FWHM) of the Stark broadening line without ionic contribution:

$$\Delta\lambda_{1/2} = 2W\left(\frac{n_e}{10^{16}}\right)\text{Å} \tag{2.5}$$

where, W is the electron impact parameters which can be selected for different temperatures, Å is the ion broadening parameter and n_e is the electron density [2.2, 2.20].

2.7 Experimental investigation in OES

A spectrograph combined with a fast detector is ideal in capturing ultra-fast transient phenomena. A system which provides a high spectral resolution of less than 0.2 nm is ideal. It has the ability to control when the spectral data was captured and for what duration is ideal in investigating the temporal and spatial evolution of plasmas. The Andor iStar Michelle ME5000 spectrograph combined with an intensified charged couple device, Andor DH734i makes an excellent combination to study laser generated plasmas. The Michelle design of the ME5000 enables a complete spectrum to be acquired simultaneously in a single shot. A wide emission range from 200 to 975 nm can be recorded simultaneously. In this way, the time needed to record a complete event is

minimized to one laser shot. The DH734i gated camera allows stable gated acquisition of 4 ns. For plasma diagnostics, this system is very suitable.

From the recorded spectrum, the transient measurements of emission from various wavelengths associated with peaks in the spectra are used to deduce the electron temperature. To measure electron density a FWHM $\Delta\lambda_{1/2}$ of a peak that is related to a particular species (e.g. CI, CII, etc) is considered. Using the measured electron density, the electron temperature can then be deduced. Another possible way to measure the electron temperature is to use the Boltzmann's distribution shown in equation 2.1. For this law, several emissions lines appearing in the spectrum which correspond to the wavelength of a particular species are used.

2.8. References

[2.1] J C Miller and R. F. Haglund, Laser ablation and Desorption *Vol*. **30** (1998).

[2.2] R. Kelly and A. Miotello, in *Pulsed Laser Deposition of Thin Films*, Eds D. Chrisey and G. K. Hubler John Wiley & Sons, New York, (1994).

[2.3] N. Konvejenic, *Phys. reports* **316** 339 (1999).

[2.4] G. Radhakrishnan, P. M. Adams and F. D. Ross, *Journal of Phys. Conf. Series*. **59** 424 (2007).

[2.5] S. Aquaviva, M. L. De Giorgi, *Appl. Surf. Scie*. 197-198 21-26 (2002).

[2.6] A. Voevodin, J. G. Jones, J. S. Zabinski, *J. Phys. Vol*. **92** No. 2 (2002).

[2.7] G. Dinescu, E. Aldea, M. L. De Giorgi, A Lunches, A Perrone, A. Zocco, *Appl. Surf. Scie.* **127** 697 (1998).

[2.8] A. Tanabashi, T. Hairao, T. Amano, *Japan* 310 (2002).

[2.9] Daniel C. Haris and Michael D. Bertolucci, symmetry and Spectroscopy "An Introduction to Vibrational and Electronic Spectroscopy" (1978).

[2.10] C. Scott, S. Arepalli, P. Nikolaev, and R. E. Smalley: *Appl. Phys.* A **72** 573 (2001).

[2.11] C. Kingston, J. Jakubek, S. Denommee, B. Simard Carbon **42** 1657 (2004).

[2.12] R.E. Smalley: *Acc. Chem. Res*. **25** 98 (1992)

[2.13] T. Ikegami, F. Nakanishi, Makoto Uchiyama, Kenji Ebihara, *thin solid films* **457** 7 (2004).

[2.14] W. Maser, E. Muñoz, A. M. Benito, M. T. Mart´inez, G.F. de la Fuente, Y. Maniette, E. Anglaret, J.-L. Sauvajol: *Chem. Phys. Lett*. **292** 587 (1998).

[2.15] G. Abdellatif, H. Imam, *Spectrochim. Acta*, Part B: Atom. *Spectrosc*. **57** 1155 (2002).

[2.16] M. Guillong, D. Günther, J. Anal. At. Spectrom. **17** 831 (2002)

[2.17] Annemie Bogaerts, Zhaoyang Chen, *Spectrochimica Acta* Part B **60** 1280 (2005).

[2.18] Wolfgang Sdorra, Jurgen Brust, and Kay Niemax, Mikrochim. *Acta* **108** 1 (1992).

[2.19] B. Dam, J. Rec& tor, M. F. Chang, S. Kars, D. G. de Groot, and R. Griessen, *Appl. Phys. Lett*. **65** 1581 (1994).

[2.20] Hans R. Griem, Plasma spectroscopy (1964).

CHAPTER THREE

3. ANALYTICAL TECHNIQUES

3.1. Plasma plume investigations by optical emission spectroscopy

The electromagnetic radiation emitted from the plume is imaged by intensified charge coupled device (ICCD)-photography and spectroscopically analysed. The spectrometer separates the unique frequencies into discrete wavelengths and quantifies the results. Figure 3.1 shows the experimental apparatus used for *in situ* time and space-resolved optical emission spectroscopic measurements at the Council for Scientific Industrial Research (CSIR). In optical emission spectroscopic (OES) investigations, a very fast-Intensified CCD camera is mounted at the exit plane of a spectrometer with a ~0.02 nm resolving power. The temporal resolution is ~2 ns. In ICCD's, such as ANDOR iStar DH734, the spectra appear at the wavelength range of about 200-950 nm. Spectra are acquired at different times by adjusting the delay times after which acquisition proceeds. In this way, spectral images of the plume can be taken spatially and temporally. Emission of carbon coming from selected excited species can be investigated by employing appropriate narrow bandpass filters to remove unwanted emssion lines.

The use of an ICCD array camera can be used to improve our understanding in nanostructure materials formed when high temperature carbon plasma condenses into carbon nanostructures such as carbon nanotubes. During adiabatic expansion, i.e. when the plasma expands as a function of time, the thermal energy is transfered into kientic energy. During this expansion, the velocities of species can be calculated. In addition to identifying the chemical species present in the plasma, changes in the mean electron temperature and the relative concentration levels of the species can

be monitored from the OES data. The electron temperature is an important plasma parameter. This is due to the fact that the electron temperature is directly proportional to the growth rate of carbon materials such as thin films. If the plasma is assumed to be in local thermodynamic equilibrium (LTE), then the electron temperature can be deduced from Saha or Boltzmann's equation. Lastly, the electron density of the emitted species can be calculated from the Stark broadening profile. It can be calculated by measuring the emitted intensity of the carbon species such as C (II) corresponding to its wavelengths such as 274.60 nm, 283.75, etc [3.1, 3.2].

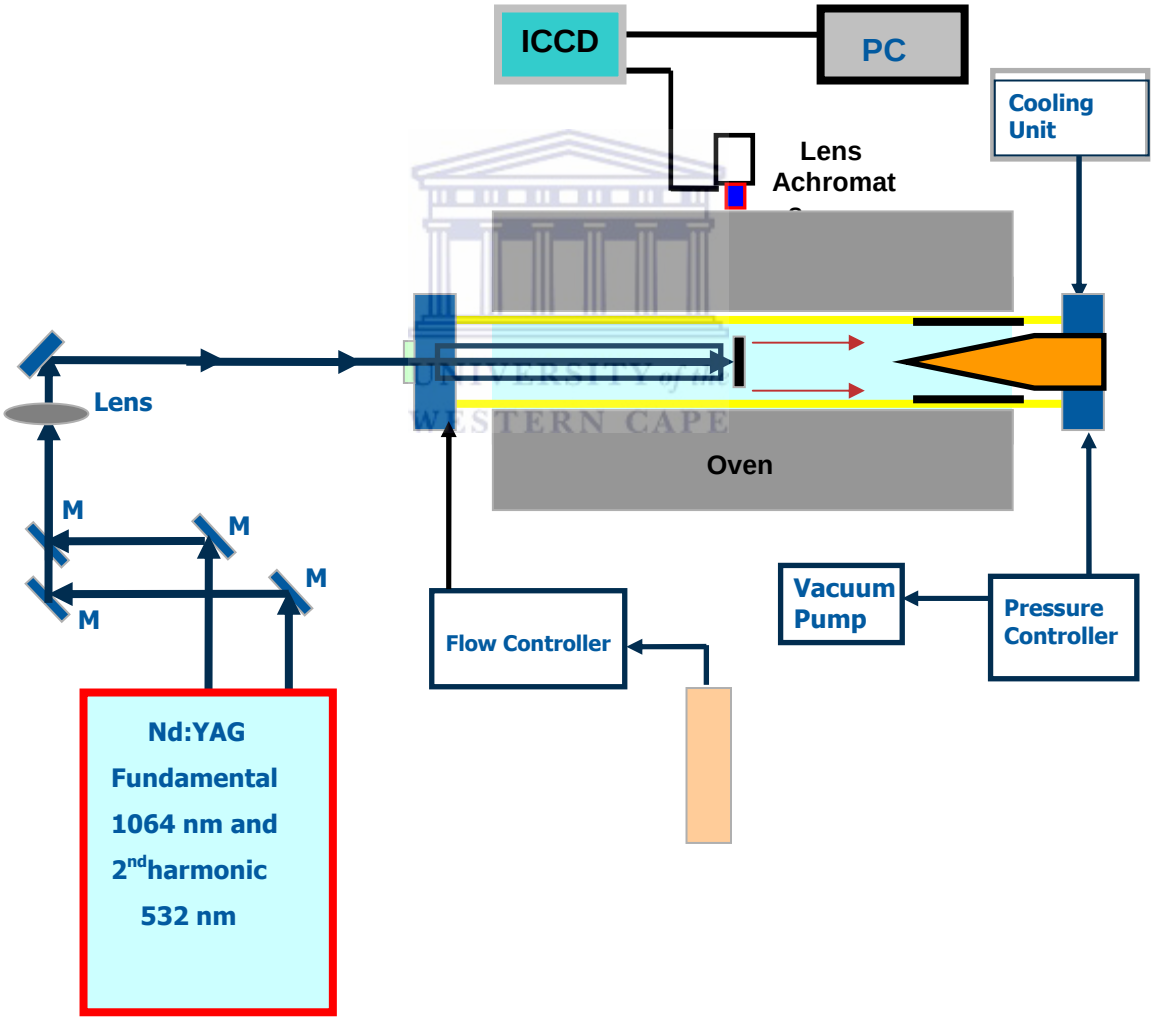

Figure 3.1: The experimental configuration for OES arranged at CSIR.

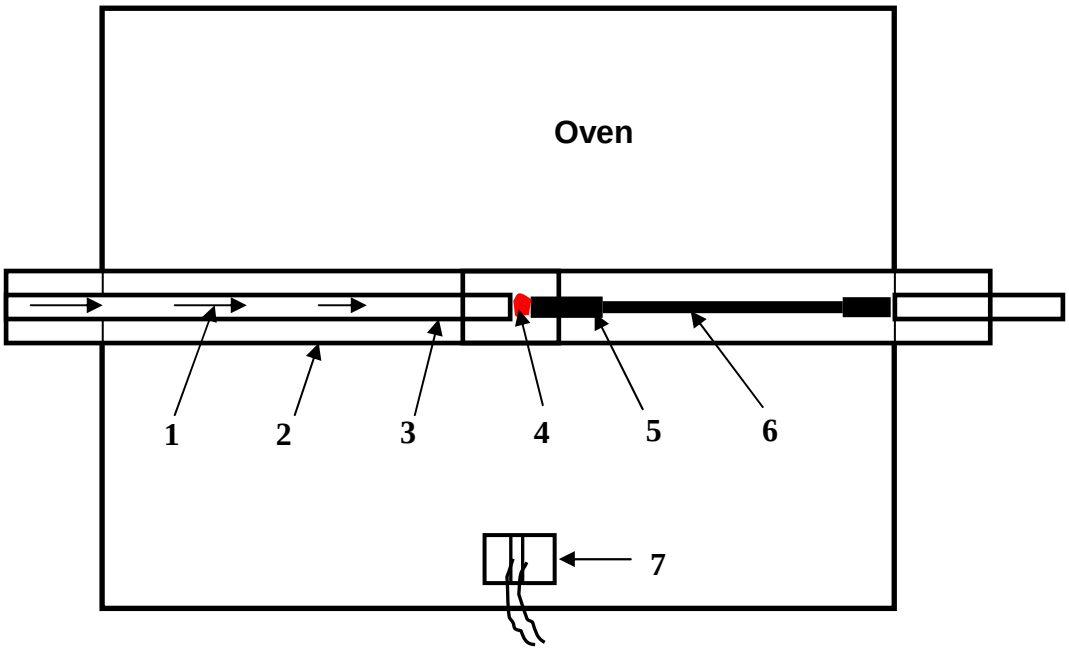

Figure 3.2: Configuration of the flow tubes and target: (1) Laser beams, (2) Outer quartz tube, (3) Inner quartz tube, (4) Plasma Plume generated when the laser beams heat the target shown in (5), (6) Stainless steel rod used to hold the target and (7) Fibre optic attached to the lens achromats and ICCD/spectrograph

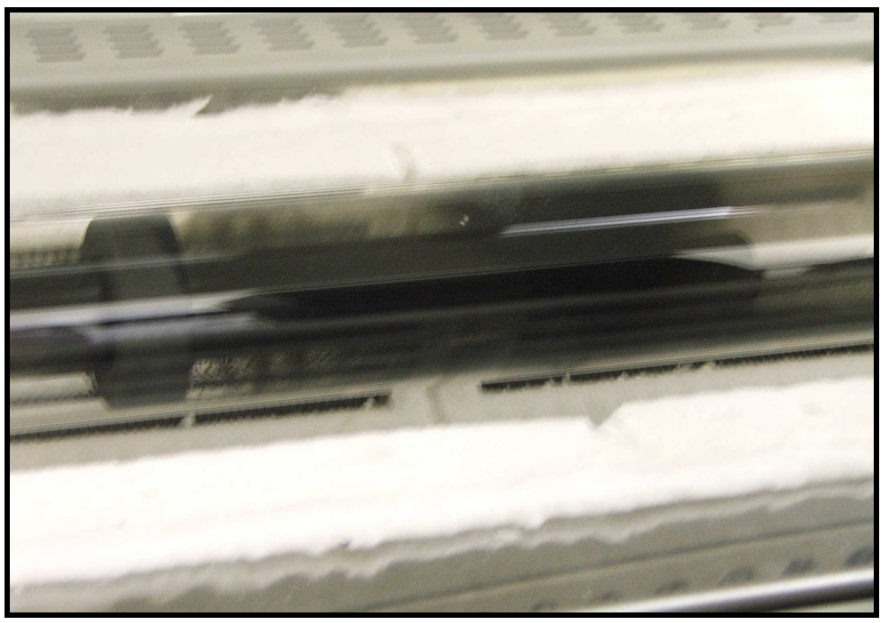

Figure 3.3: A Photograph of an open laser-ablation oven showing the target as well as the inner and outer quartz tubes.

In order to identify the chemical content of the plume, a spectrometer is employed. By allowing the broad emission light emission from the plume to be collected by lenses which then focus the light on a set of prisms which spread the light into its exact components by making use of the fact that different wavelengths refract differently when entering a refractive medium. In this way we are able to separate light of different wavelengths emitted simultaneously and at different times. These can be multiple emissions of a single element in its different ionization stages and as well as from multiple elements depending on the composition of the target. In this way, the elemental composition of the target which is vaporized by the laser can be tracked; hence the temperature and densities can be calculated. Figure 3.1 shows a schematic diagram of how the emission of the plume from an ablated target is collected and transferred to the Andor Spectrograph/ICCD system. Figure 3.4 shows the emission intensity lines of Carbon, Yttrium, Nitrogen and Nickel detected at 1000 ℃ and the pressure of 400 Torr, 200 sccm, using the setup shown in Figure 3.1. The spectrum indicates that Y and Ni are more excited at the wavelength range between 450 nm and 600 nm.

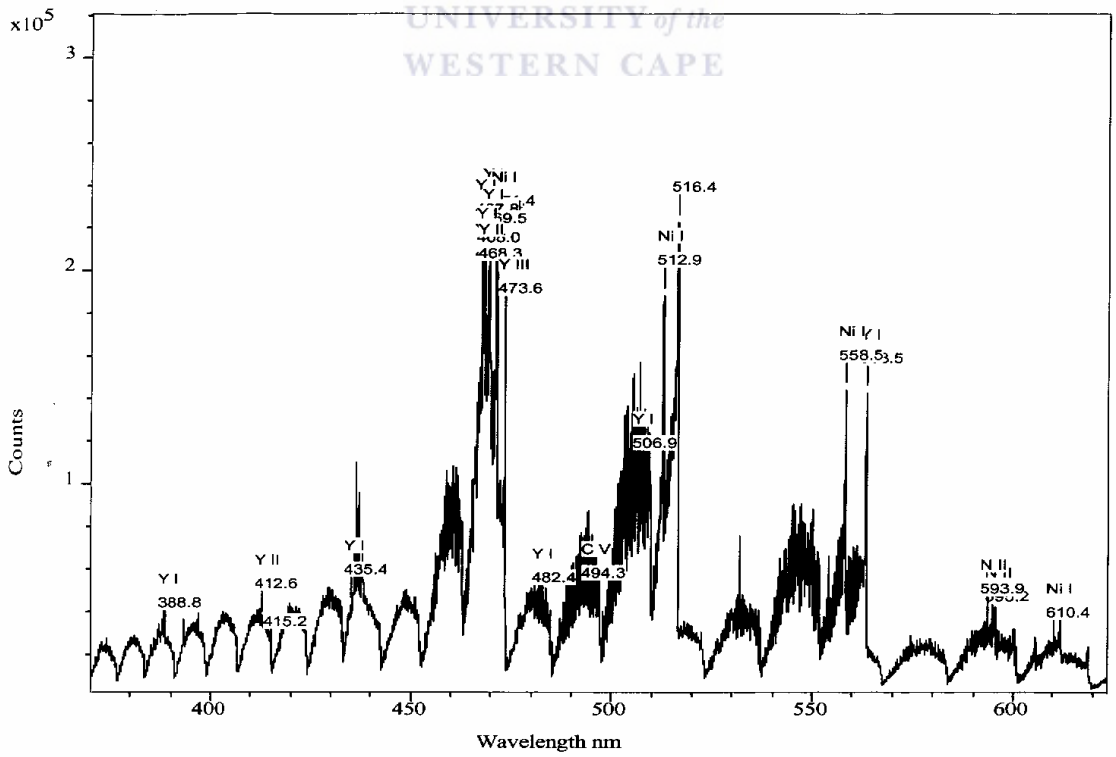

Figure 3.4: Emission spectrum of Carbon lines detected by an ICCD at different wavelengths.

3.2. EXPERIMENTAL PROCEDURE

3.2.1. OES studies of graphite composite targets ablated in argon

The experimental set-up employed for spectroscopic investigations is shown in Figure 3.1. The target was irradiated with the Q-Switched Nd: YAG laser operating at the wavelengths of 532 and 1064 nm, in the quartz tube. The target used for this study was made by compressing a paste containing high purity graphite, metal catalysts (4% Yttrium and 1% Nickel) and Dylon carbon cement. The energy densities of the lasers were 12.75 $J.cm^{-2}$ and 76.4 $J.cm^{-2}$, respectively. The 532 nm laser beam was routed by reflection via two 45º mirrors coated for 532 nm while the 1064 nm was also routed by reflection via two 45º mirrors coated 1064 nm. The second mirror from of 532 nm transmitted 1064 wavelength while reflecting the green beam (532 nm), since it was coated of 532 nm and 1064 nm. The lens was placed 1.5 m away from the target to focus the beam towards the target. The last mirror transmitted both 532 and 1064 nm wavelengths. The outer and inner quartz tubes used had an outer diameter of 50 mm and 26 mm, and inner diameter of 45 mm and 23 mm, with a length of about 1.5 m and 0.7 m. The inner quartz tube was supported by graphite discs as shown in Figure 3.3. The target was mounted on the stainless steel rod which was placed at the centre of the outer quartz. The Quartz tubes were enclosed within a hinged Carbolite furnace as shown in Figure 3.1 and 3.3. The flow and pressure of argon gas within the quartz tube were controlled by MKS 247 pressure controller and Flow meter. The flow of Ar gas was set at different pressures and flow rates of 150 sccm and 200 sccm as shown in Table 3.1. In brief, the flow rate was kept at 150 and 200 sccm while the pressure was varied in both flow rates. To ablate the target, the furnace temperature was set at 1000 ˚C. The spatial distributions of emitting species were obtained for different times following the laser pulse using the Andor iStar ME 500-DH734 spectrograph intensified coupled charge device (ICCD) attached to the spectrograph. The ICCD consisted of an 18 mm diameter Micro Channel Plate (MCP) image intensifier coupled to a 1024 ×

1024 pixels CDD by a high quality relay lens system. The lens acromats (Andor ME OPT-0007) was located outside the furnace, approximately 28 cm away from the target surface. The position of this device was optimised for maximum light detection with an aid of a red laser diode (HeNe) mounted collinearly with the lens achromat mount.

Measurements were performed by opening the furnace for short periods up to 6 seconds to capture ablation events. For each measurement, the average of three laser shots was recorded. Laser shots were taken each time in intervals, Δt, of 100 ns in the range of 0 to 1.2 µs. This was repeated 10 times, while the distance from the target surface was varied from 0 to 5 mm. The exposure time, which is the time during which light is allowed to fall on the CCD sensor prior to readout, was set to 0.05 s while the Micro-Channel Plate (MCP) gain which enhances the CCD sensor was kept at 80s, to increase the voltage across the MCP in order to enhance (or amplify) the CCD sensor. The digital delay generator (DDG) built into the Andor iStar DH-734 detector head was used by activating the external source from the trigger pulse to control the intensifier tube for gating applications. The insertion delay or propagation delay, which is the length of time taken for a trigger pulse to travel through the DDG and gater so that the intensifier tube is turned on, was set to normal. A delay pulse generator was used to trigger the laser to fire and to control the gate width i.e. the length of time that the intensifier tube is kept on the ICCD during which the camera collects spectra. The temperature of the CCD was kept at ~ -10°C to reduce the dark current and to improve the signal to noise ratio. This was done to remove noise in the signal which is attributed to the continuum signal emitted.

After each data acquisition, the temperature of the furnace dropped by about 6 ^{0}C due to heat loss caused by the surroundings while furnace was opened. The furnace was then allowed to regain its setting before the next measurement commenced. To ensure that the camera was reporting true results, it was calibrated before-hand by using a mercury lamp. Figure 3.5

shows the Andor iStar ME5000+DH734 ICCD detector and the lens achromats that were used at CSIR to detect the elemental species or to collect the spectra.

Figure 3.5: An Andor iStar ME5000+DH73 intensified Charge couple device used during laser ablation.

Table 3.1: Summary of pressures used to ablate the target at a temperature of 1000 ºC

Pressure (Torr)
100
400
600

3.2.2. Carbon nanotubes synthesis

To synthesize carbon nanotubes (CNTs), the same parameters used in OES work were applied. The laser was allowed to continuously ablate target at a repetition rate of 30 Hz. The target was rastered in a spiral shape to avoid drilling the target. In each experimental condition, the laser was operated for about 90 minutes. After this time, the synthesized materials were scrapped off the inside of the outer quartz tube for analyses.

3.3. RAMAN SPECTROSCOPY

3.3.1. Introduction

When a beam of light is passed through a transparent substance small amount of the radiation will be scattered. If a monochromator or radiation of a very narrow frequency band is used the scattered energy will consist almost entirely of radiation of the incident frequency. Such process is called Raleigh Scattering. But if the beam is scattered certain discrete frequencies above and below that of the incident, then the process is referred as Raman scattering [3.3].

Ever since its discovery, by Raman and Krishnan in 1928, Raman spectroscopy has been a widely used tool to characterize material composition, sample temperature and strain from the analysis of the materials phonon modes. [3.4]. In this study the Raman technique will be used to identify the quality of the tube and tube type i.e. if it is MWCNT or SWCNT and if it is SWCNT, then the tubes are metallic or semiconductor in nature.

3.3.2. Characterization

3.3.2.1. Raman active modes in carbon materials

In carbon nanotubes, the most prominent modes are the G-band (G-graphite), the D-band (D-disorder) and the G'-band (second-order Raman scattering from D-band vibrations). Another important and unique feature is the radial breathing mode (RBM) which occurs only for SWCNTs. RBM has a frequency that is inversely proportional to the diameter of the tube which makes it very convenient to measure the tubes diameter.

3.3.2.2. Radial breathing mode

The RBM is unique feature to SWCNTs mode. The RBM in carbon material occurs in radial direction and is analogous to tubes breathing in and out. RBM frequency (ω_{RBM}) which is given by:

$$\omega_{RBM} = \frac{A}{d_t(nm)} + B(cm^{-1}) \qquad (3.6)$$

where the constants A and B are determined experimentally and d_t is the diameter of the tube [3.5]. These values have been determined experimentally to be A = 248 cm^{-1}nm and B = 0 for isolated SWCNTs on a SiO_2 substrate. The RBM in SWCNTs is found between the frequencies of about 200 and 500 cm^{-1} as shown in Figure 3.6. Raman spectrum is observed for the intermediate frequency modes (IFM) which lie between the RBM and the G-band features and the ITOLA is the second order modes i.e. the combinations of optical and acoustic modes.

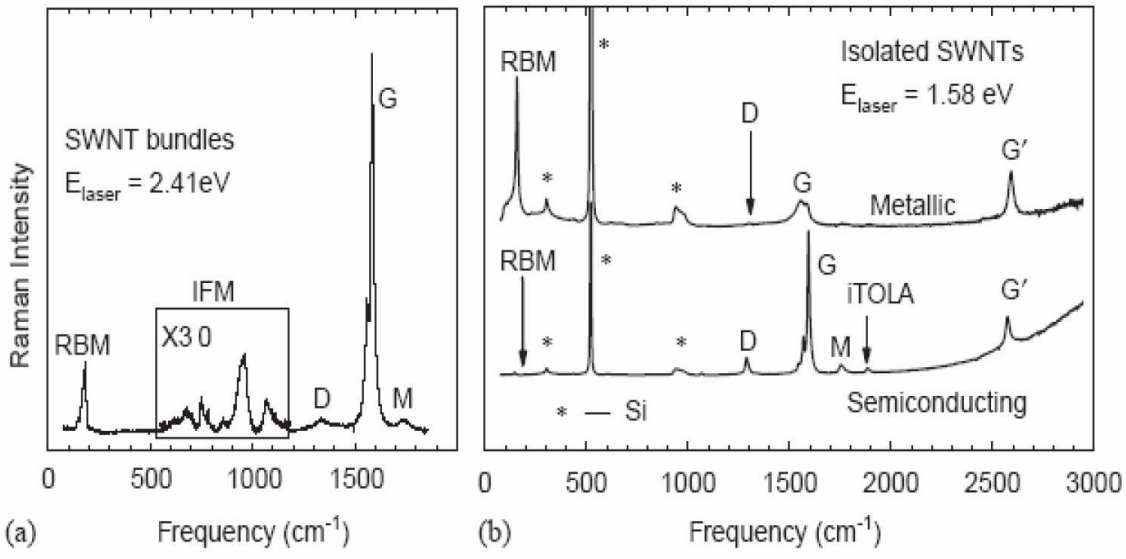

Figure 3.6: Raman spectra of SWCNTs [3.5].

3.3.2.3. The tangential mode

In carbon atoms, the G-band is related to the tangential shear mode. However, in graphite there is one single G-mode at about 1580 cm^{-1}, while in CNTs, the single G-band transforms into wave-vectors along the circumference. This G-band is an intrinsic feature of CNTs, which is closely related to vibrations in all sp^2 carbon materials. However, the G-band in SWCNTs is not dispersive and hence, its frequency is not sensitive to laser energy as in other sp^2 carbons [3.6]. Analysing the Raman spectra of this band one can characterize diameters and also differentiate between the semi-conducting and metallic SWCNTs as shown in Figure 3.6. In the case of semi-conducting nanotubes, the highest mode, G^+ at between 1590-1595 cm^{-1} is a longitudinal optical (LO) shear mode parallel to the axis of the nanotube, while G^- is the transverse optical (TO) shear mode perpendicular to the tube axis. The G^-modes are "softer" due to the higher curvature or tubes of smaller diameters. However, for metallic tubes, the down shift frequency of the G^- mode is strong for metallic nanotubes. Hence the down shift of the G^- mode for small diameter tubes is found in the frequency of about 100 cm^{-1}. Furthermore, the G^- energy decrease with decrease in diameter is faster for metallic tubes than when compared to the semi-conducting nanotubes, the G^+ remains constant in frequency [3.7].

3.3.2.4. The D and G' mode

The D-band is defined as the defect mode since it arises only if there is a defect in the carbon materials e.g. CNTs, while the G'-band is an intrinsic property of the nanotube and graphite. The D-band is present in all carbon allotropes (e.g. diamond, graphite, CNTs, etc), including amorphous sp^2 and sp^3 carbon but only if there are defects. While G' band, is present in defect-free nanotubes. Figure 3.6 shows the D-and-G' band features which are observed in Raman spectra of semi-conducting and metallic SWCNTs at the single nanotube level. The D-band's frequency arises between $1250 < \omega_D <$

1450cm^{-1}, while the G' band's frequency arises between 2500 < $\omega_{G'}$ < 2900 cm^{-1}. Therefore, the frequency of G'-band is twice the D-band frequency. The D-and-G' band are sensitive to the diameter and chirality of SWCNTs. Therefore, this denotes that the frequencies ($\omega_{G'}$ and ω_D) are both dependent on the diameter and chiral angle, whereas the ω_{RBM} and ω_G do not show any significant dependence on the chiral angle [3.7]. Figure 3.7 shows two G'-bands peaks observed at different energies from the same nanotube, this occurs only if the incoming and the scattered light can both be resonant with two different energies from one particular nanotube [3.8]. Table 3.2 shows the summary of the modes found in SWCNTs.

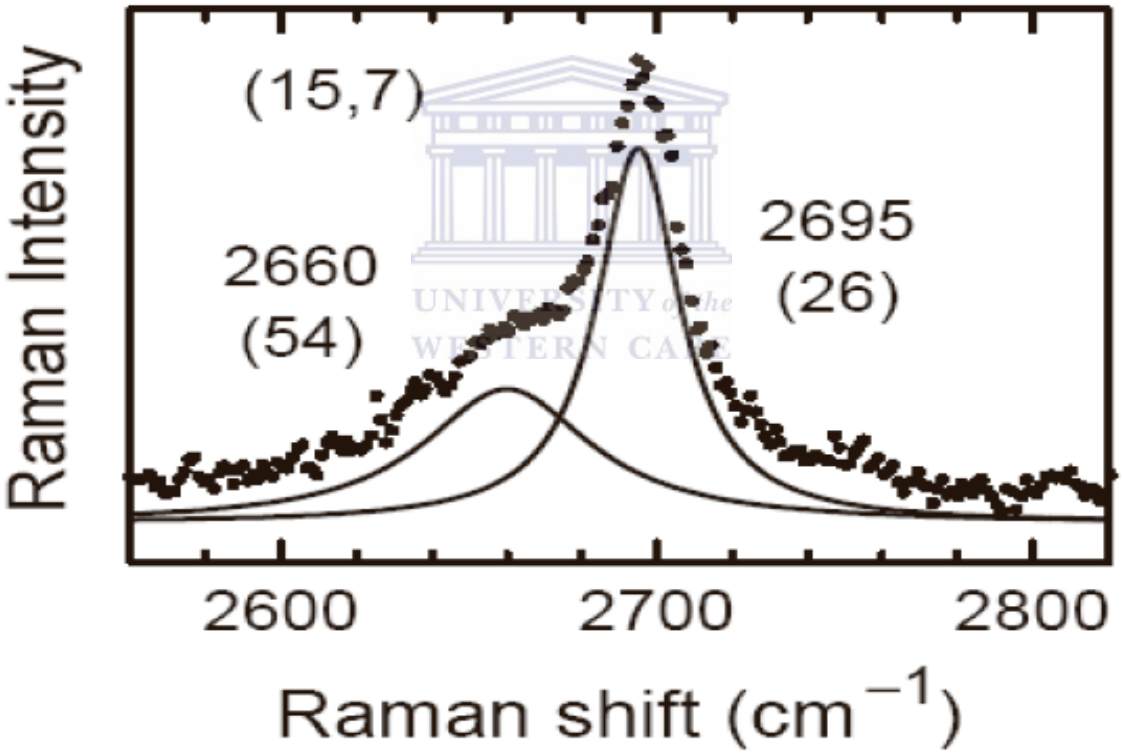

Figure 3.7: Two G' peaks from a (15, 7) nanotube; where the incident E_L = 2.41 and the scattered $E_L - E_G$ = 2.08 eV light [3.8].

Table 3.2: Vibrational modes observed by Raman scattering spectroscopy in SWCNTs [3.6].

Notation	Frequency (cm^{-1})	Symmetry	Type of mode
RMB	$248/d_t$	A	In phase radial displacement
D-band	~1350	-	Defect-induced dispersive
G-band	1550-1605	A, E_1, E_2	Graphite-related optical mode
G'-band	~2700	-	Overtone of D-band highly dispersive

- The related 2D graphite mode has *E* symmetry. In 3D graphite, the corresponding mode is denoted by E_{2g2}

3.4. ELECTRON MICROSCOPE

Electron microscopy (EM) is one of the techniques that are used extensively by researchers to investigate nanomaterials. The EM uses electrons with high energy and focuses them with magnetic lenses. In the electron microscope, both photon and electron signals are generated as a finely focused electron beam strikes a given sample. The signals detected in the electron microscope are shown in Figure 3.8. The analysis of these signals provides visual and chemical information about the specimen. Any information about the specimen composition can be determined using characteristic X-rays, Auger electrons and cathodoluminescence [3.9, 3.10].

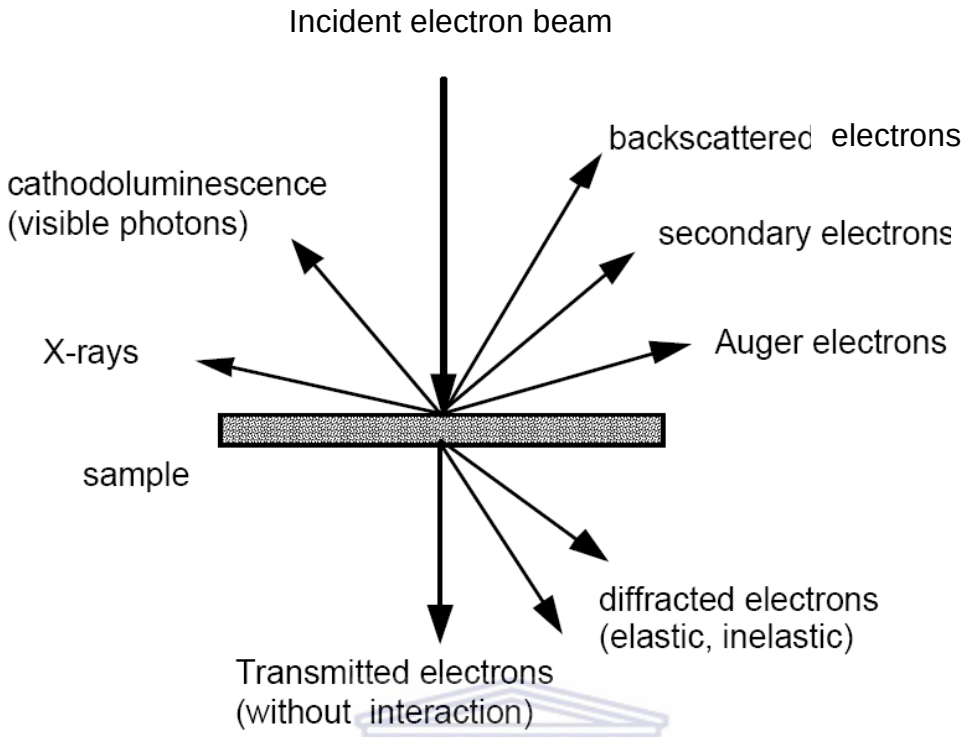

Figure 3.8: Schematic diagram of the signals generated during the primary electron beam – specimen interaction [3.9, 3.10].

3.4.1. SCANNING ELECTRON MICROSCOPE

3.4.1.1. Introduction

In a typical SEM, electrons are thermionically produced from a tungsten (W) or lanthanum hexaboride (LaB_6) cathode filament or via field emission. The electrons are accelerated in the direction of the anode. Tungsten is often preferred because it has a high melting point and it is the metal with the lowest vapour pressure of all metals, which allows it to be heated to high temperature for the emission of electrons. The beam of electrons is created which have energies ranging from a few hundreds electron volts (eV) to 40 keV. This beam is collimated by electromagnetic condenser lenses and directed towards an anode stage. An objective lens is used to focus further to

a small diameter spot size and then scanned across the surface of the sample by electromagnetic deflection coils. The incident electrons interact with the sample and this primary electron beam effectively spreads and forms below the surface of a teardrop-shaped volume. This volume is known as interaction volume, which extends from less than 100 nm to ~5 μm into the surface depending on the atomic mass, atomic number and accelerating voltage. The scattering process occurring in the sample leads to the emission of electrons in this region which are then detected to produce an image. The interaction of electrons also leads to the production of x-rays, which may be detected in an SEM equipped for energy dispersive X-ray spectroscopy (EDS) or wavelength dispersive X-ray spectroscopy (WDS). The EDS is useful for obtaining rapid qualitative analysis as well as quantitative analysis of an unknown sample, while WDS is useful for obtaining qualitative information and analysis of light or trace elements [3.9]. Table 3.3 shows (or summarises) the nature of information obtained from different materials as well as the resolution that applies to each signal.

Table 3.3: Basic SEM modes of operation [3.9].

Signal/mode	Information	Material	Resolution
Secondary electrons (SE)	Surface Morphology	All (*)	~1nm
Backscattered electrons (BSE)	Atomic number and surface morphology	All (*)	0.1-0.5μm (**)
X-ray (EDS or WDS)	Atomic composition	All (flat)	~1μm
Cathodoluminescence (CL)	Bandgap, impurities, lifetimes	Insulators and semi-conductors	Several μm's

(*) usually sizes of 1cm, dependent on SEM configuration,

(**) voltage and Z dependent

3.5. References

[3.1] H. R. Griem, *Plasma Spectroscopy* ~McGraw-Hill, New York, (1964).

[3.2] D. B. Chrisey and G. K Hubler. Pulsed Laser Deposition of thin films, (1994).

[3.3] C.N Banwell, Fundamentals of Molecular Spectroscopy, 3rd Edition. (1983).

[3.4] David L. Andrews and Andrey A. Demodov, an Introduction to Laser Spectroscopy, 2nd Edition (2002).

[3.5] M. S. Dresselhaus, G. Dresselhaus, R. Saito and A. Jorio, Physics Reports, **409** 47 (2005).

[3.6] M.S. Dresselhaus, G. Dresselhaus, A. Jorio, A.G. Souza Filho, R. Saito, Carbon **40** 2043 (2002).

[3.7] A Jorio, M A Pimenta, A G Souza Filho, R Saito, G Dresselhaus and M S Dresselhaus, *New Journal of Physics* **5** 139.1 (2003).

[3.8] A.G. Souza Filho, A. Jorio, Anna K. Swan, M.S. Ünlü, B.B. Goldberg, R. Saito, J.H. Hafner, C.M. Lieber, M.A. Pimenta, G. Dresselhaus, M.S. Dresselhaus, *Phys. Rev. B* **65** 085417 (2002).

[3.9] D. Chescoe and P. J. Goodhew, The Operation of Transmission and Scanning Electron Microscopes, (1990).

[3.10] P. J. Goodhew and F. J. Humphreys, Electron Microscopy and Analysis, 2nd Edition, Taylor & Francis, London (1988).

CHAPTER FOUR

4. RESULTS AND DISCUSSIONS

4.1. PLUME COMPOSITION DETECTED IN ARGON

The experimental set-up described in chapter three allowed us to obtain spectra at different time delays and distances from the target surface. The spectrum in Figure 4.1 shows elemental species observed in the wavelength range of 300 to 700 nm from the plasma plume; at the pressure of 400 Torr and flow rate of 200 sccm. The emission lines of C_2 Swan bands and Deslandres D' Azambuja systems having their electronic transition $C^1\Pi_g$ - $A^1\Pi_\mu$, and d3Πg - $a^3\Pi\mu$ were detected. However, we have not observed any distinct peak attributable to C_3 in the spectrum, but only an underlying continuum. Elements such as Nickel and Yttrium which were mixed with pure graphite to act as catalysts in single wall carbon nanotubes synthesis were also identified. Other carbon species such as C (I), C (II), C (III), C (IV), C (V), and the emission lines of oxygen and nitrogen were also observed. These lines can be explained by the fact that the metal salts were prepared from nitrates. Out-gassing of the targets was not fully completed to remove N_2 and O_2. The emission lines of Yttrium are more dominating in the spectrum. However, as the pressure was increased from 400 to 600 Torr, the intensity of argon emission lines increased and was larger in magnitude than those of Yttrium.

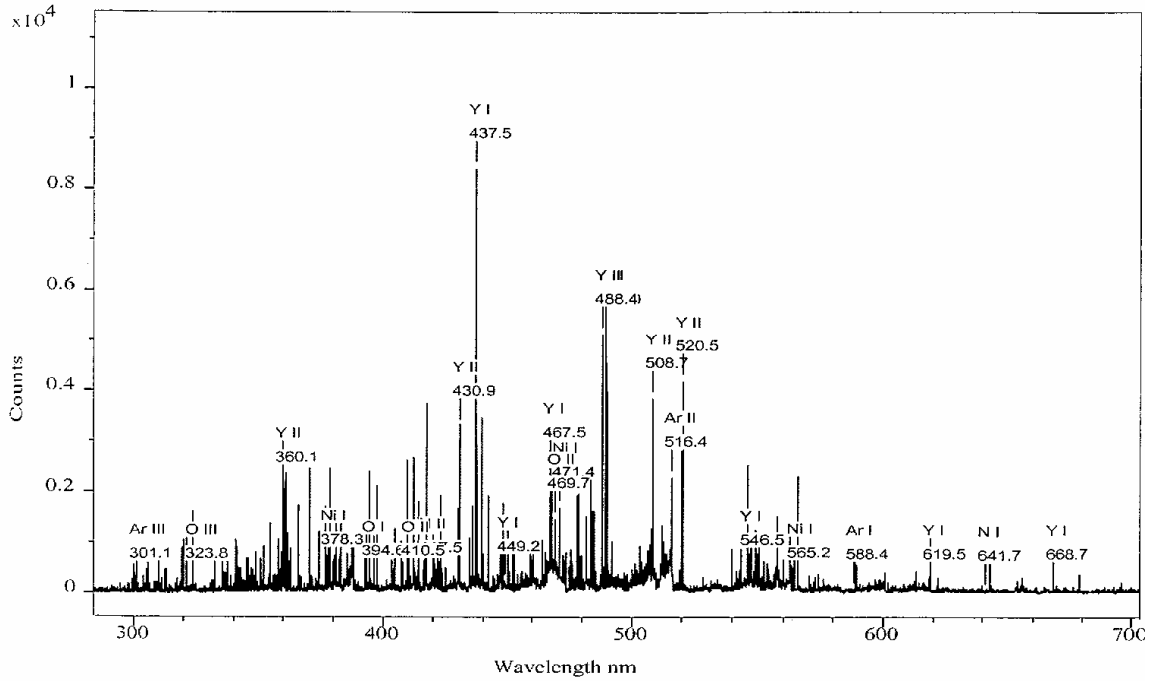

Figure 4.1: The ICCD spectrum observed at the wavelength range of 350-700 nm, during the ablation of graphite/catalyst target in an Ar gas.

Figure 4.2 (a-d) compares the optical emission spectra recorded from the plasma plume viewed from the side at a distance of 1 mm from the target surface. Laser energy density of 12.8 J.cm^{-2} and 76.4 J.cm^{-2} at 532 and 1064 nm was used to ablate the graphite composite target consisting of 4% Y, 1% Ni and 95% C. The optical emission spectra were recorded at different pressures. The integration time was set to 100 ns and a delay time of 100 ns was used. Ar flow rate was fixed at 200 sccm. At 100 and 400 Torr, as shown in Figure 4.2(a) and (c) respectively, the intensity of the atomic emissions lines of C, Y and Ni increases as well the C_2 Deslandres D' Azambuja system. The fluctuations in the intensity of the emissions lines are more clear in Figure 4.3, 4.4 and 4.5 where the emission lines of C_2 Deslandres D' Azambuja system, Ni and Y are plotted as a function of pressure at different distances from the target surface. In these plots the damped oscillatory behaviour of the emission intensities is observed. Combinations of processes simultaneously contribute to this behaviour. These are:

- Ar gas pressure, flow rate and its atomic mass,
- The kinetic energy of the ablated species,
- The temperature of the furnace,
- Pressure attributed to the plasma plume wave front.

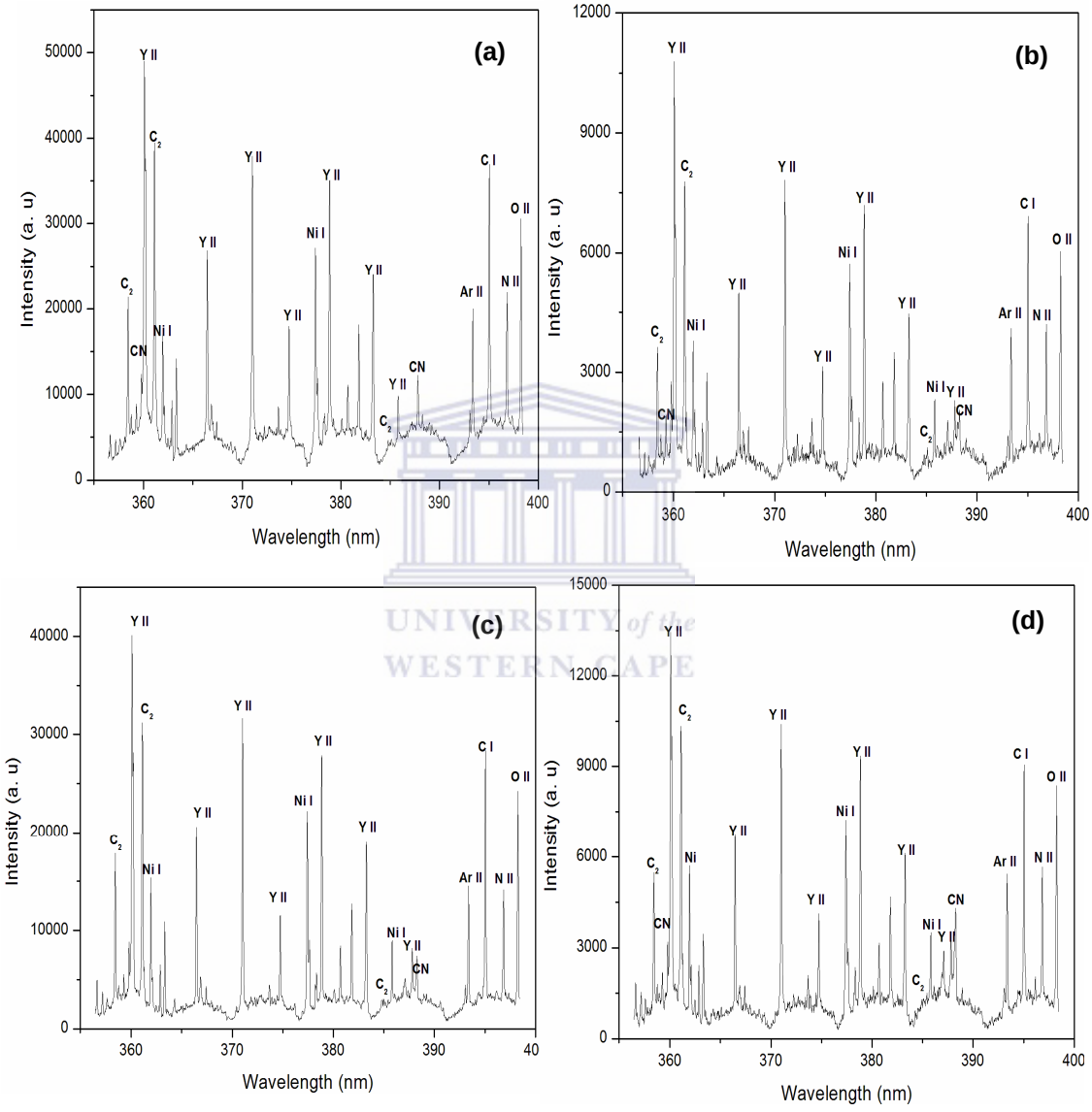

Figure 4.2: The emissions spectra recorded during the ablation of graphite composite targets in the wavelength region of 355-400 nm with the delay time of 100 ns and flow rate of 200 sccm: (a) 100 Torr, (b) 200 Torr, (c) 400 Torr and (d) 600 Torr.

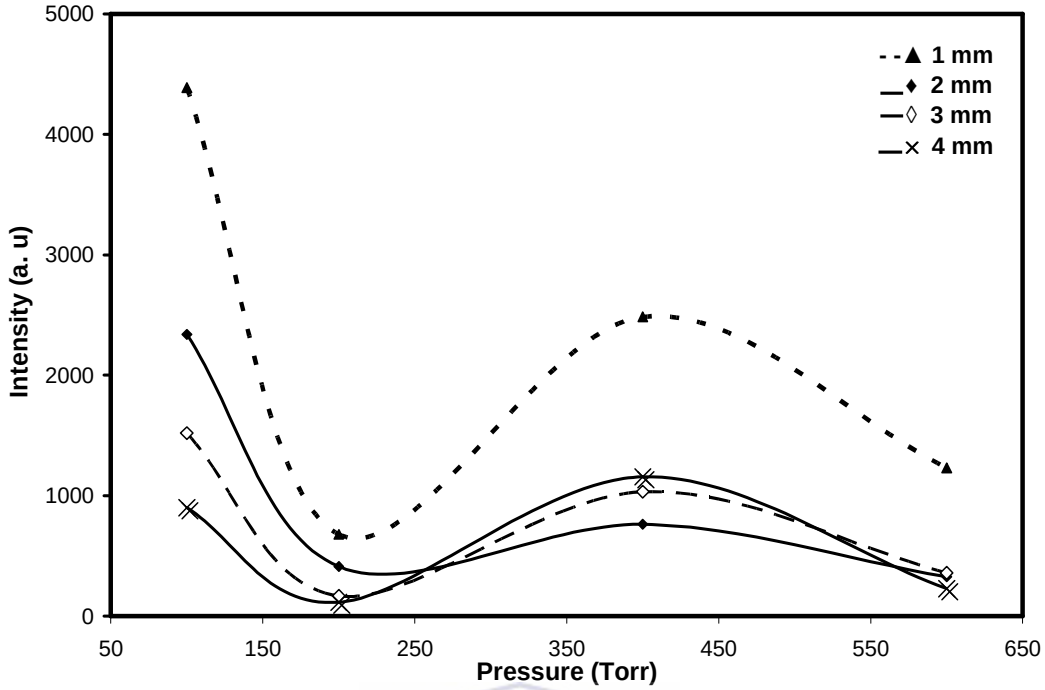

Figure 4.3: The emission intensity as a function of pressure associated with C_2 Deslandres D' Azambuja at the wavelength of 385.22 nm, at different distances and at the fixed flow rate of 200 sccm.

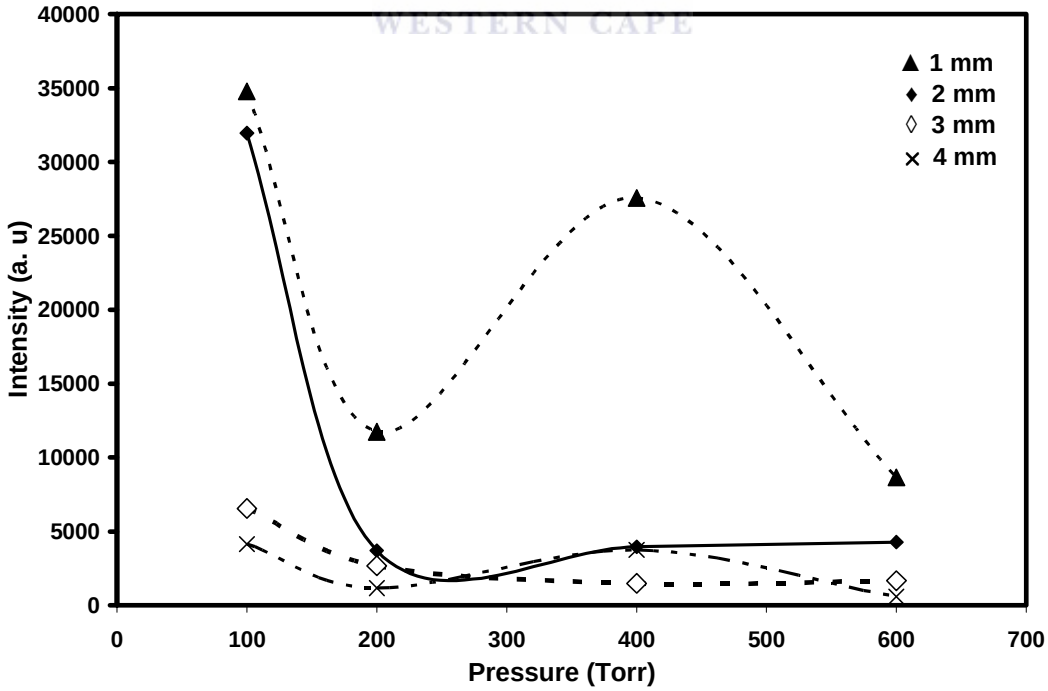

Figure 4.4: The emission intensity as a function of pressure associated with Yttrium at a wavelength of 437.5 nm, at different distances and at the fixed flow rate of 200 sccm.

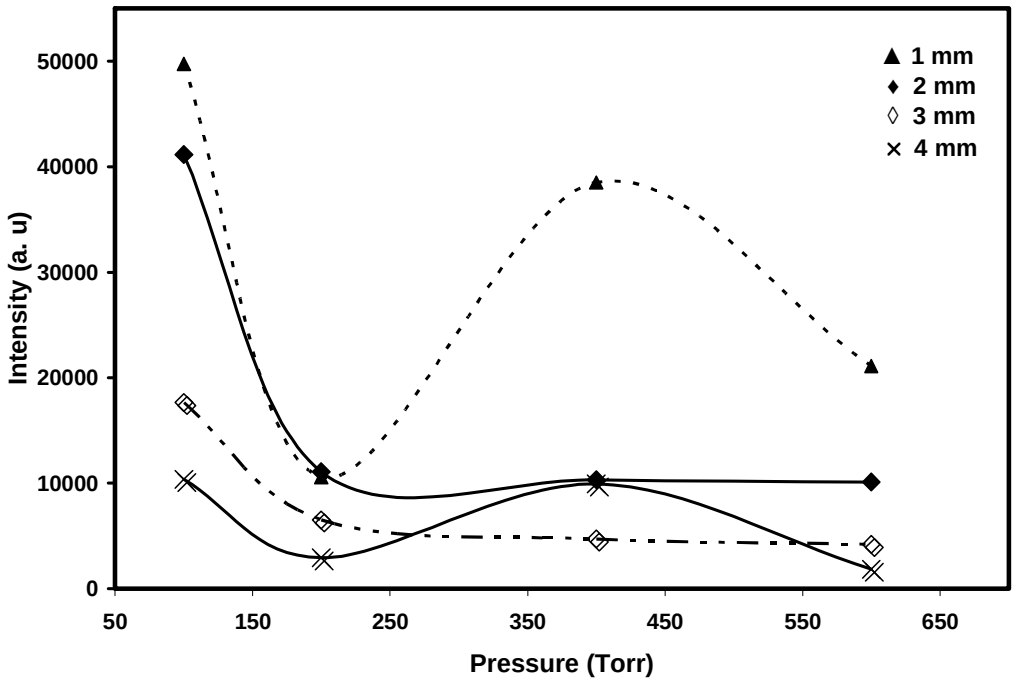

Figure 4.5: The emission intensity as a function of pressure associated with Nickel at a wavelength of 361.1 nm, at different distances and at the fixed flow rate of 200 sccm.

The spectra in Figure 4.6 show the characteristic Swan bands system of C_2 with a vibrational sequence $\Delta V = 0$, at pressures of 100, 200, 400 and 600 Torr. Unlike in the Deslandres D' Azambuja system shown in Figure 4.2, the line intensities decrease with increasing pressure. In Figure 4.6 (b-d), the C_2 intensity decrease due to the cooling of the plume which is caused by the pressure increase. In (d) the intensity of C_2 increases as the distance from the target surface increases from 0 to 2 mm and decreases as the distance increases further [4.1]. Table 4.1 shows the main emission lines of carbon species and the vibrational transitions of the identified molecular species detected during graphite ablation in an argon gas.

Table 4.1: Main Carbon emission systems and vibrational bands recorded during laser irradiation.

Species	λ (nm)	Vibrational bands	Systems	Transitions
C I	247.86			$3\ s^1P^o_1 \rightarrow 2p^2\ ^1S_1$
C I	394.22			$6p^1S_0 \rightarrow 3s\ ^1P^o_1$
C II	274.60			
C II	283.75			
C II	387.61			
C II	387.62			
N II	488.00			
O	310.00			
Ni I	279.86			
Y I	437.50			
Ar II	516.40			
C_2	516.52	(0, 0)	Swan	$d\ ^3\Pi g\text{-}a\ ^3\Pi\mu$
	512.93	(1, 1)		
	509.77	(2, 2)		
C_2	385.22	(0, 0)	Deslandres D' Azambuza	$C\ ^1\Pi_g - A\ ^1\Pi\ \mu$
	358.76	(3, 2)		
CN	388.30	(0, 0)	Violet	$B\ ^2\Sigma^+ \text{-} X^2\ \Sigma^+$
	358.39	(3, 2)		
	358.59	(2, 1)		

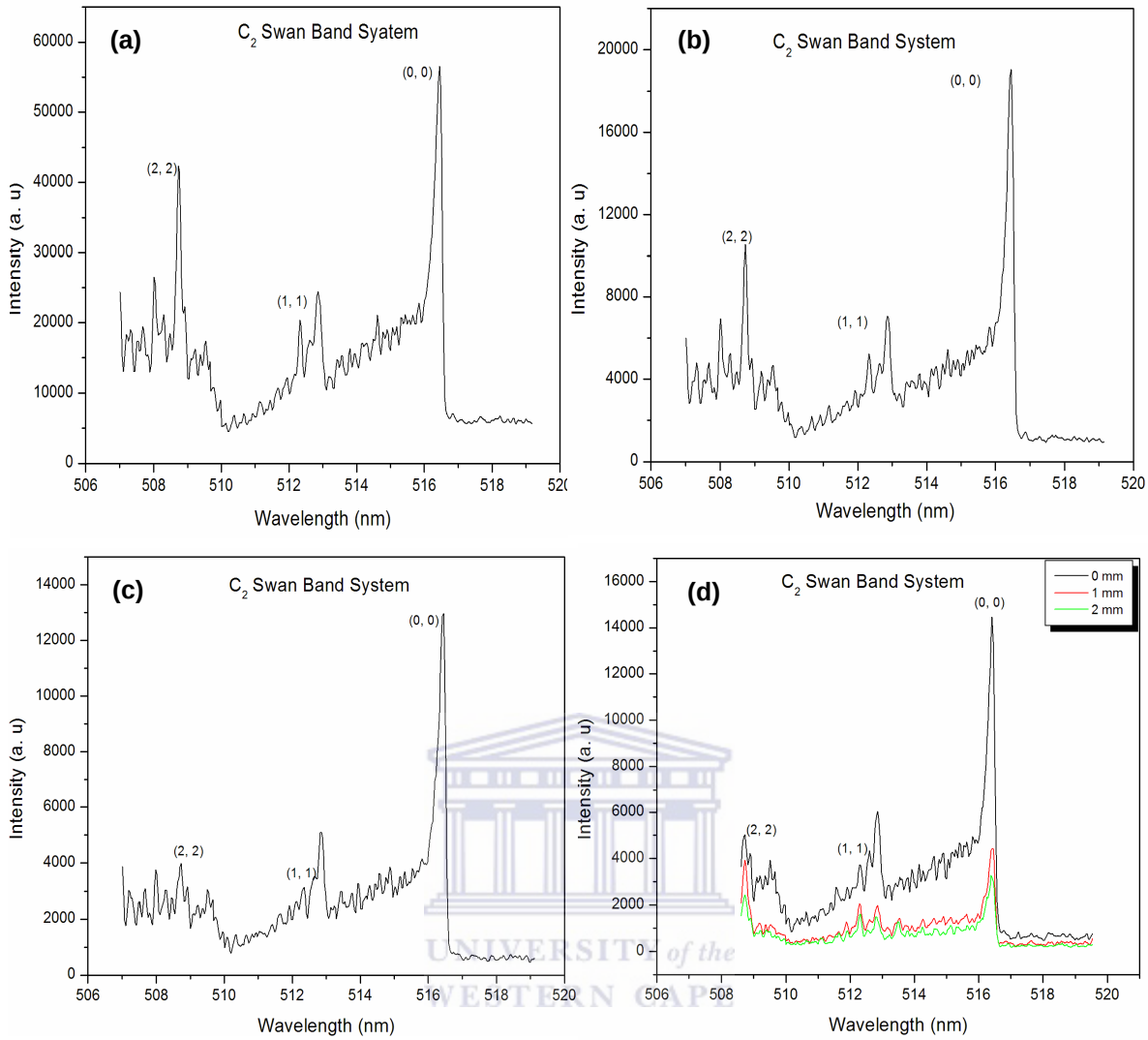

Figure 4.6: Typical emission of C_2 Swan band system recorded at different pressures: (a) 100 Torr, (b) 200 Torr, (c) 400 Torr and (d) 600 Torr at a gradual distance increase between 0-2 mm and at a fixed flow rate of 200 sccm. The time delay used is 100 ns while distance used in (a)-(c) is 1 mm from the target surface.

4.1.1. The temporal and spatial behaviour of the plume emissions

Figure 4.7shows the spatial evolution of C_2 Swan bands ($d^3\Pi g \rightarrow a^3\Pi u$) at different pressures and flow rates. In (a), the emission of C_2 Swan bands at 100 Torr are more intense than at other pressures. At 100 and 400 Torr, C_2 Swan bands oscillate in the same fashion. It is clear that between 0 and 2 mm distance from the target surface the intensity of C_2 Swan increases. At further

distances such as 3, 4 and 5 mm away from the target surface, the intensity of C_2 Swan band decreases almost exponential due to the recombination as well the plasma cooling, as it expands adiabatically. In Figure 4.7(b) the intensity of Swan band systems at 400 Torr are more dominating than at 100 and 600 Torr. At 600 Torr the C_2 Swan bands behave the same irrespective of the flow rates. Moreover, the intensity of C_2 in (b) is higher closest to the distance from the target surface and reduces rapidly as the distances increases. The decrease in C_2 is more or less smoother. The decrease in the intensity of C_2 at larger distances is due to the plasma cooling caused by recombination. These changes observed in the intensity reflect the evolution of the plume composition.

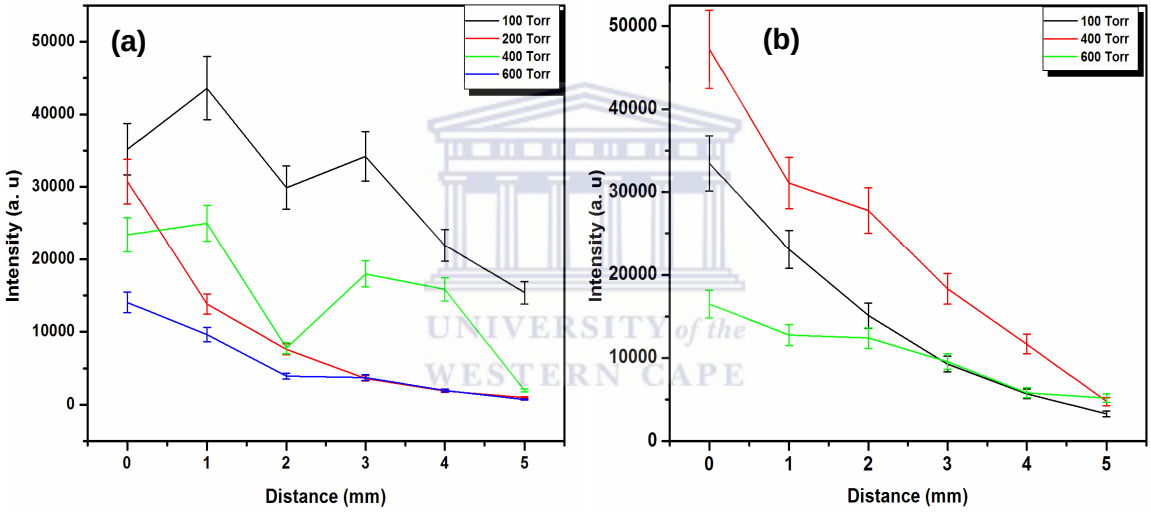

Figure 4.7: The variation in C_2 Swan band intensity at 316.5 nm with distance, at different Ar pressures and flow rates of 150 and 200 sccm.

The temporal distributions of emission intensities of C_2 Swan band and C (I) at 1 mm distance from the target surface are plotted in Figure 4.8 for different pressures. Each profile is normalised to its peak value. In this figure the arrival velocities of C_2 and C (I) are calculated at 1 mm distance at different times, at the pressure of 100 and 600 Torr. Therefore using $v = s/t$, where v is velocity, s is the distance and t is the time, then the times related to the peak positions are respectively ~1.0×10^4 ms^{-1}, 2.5×10^3 ms^{-1} and 2.5×10^3

ms^{-1}, 2×10^{3} ms^{-1}. This shows that C_2 Swan band ($d^3\Pi g \rightarrow a^3\Pi u$) travels with higher velocity in the plume than as compared to C (I).

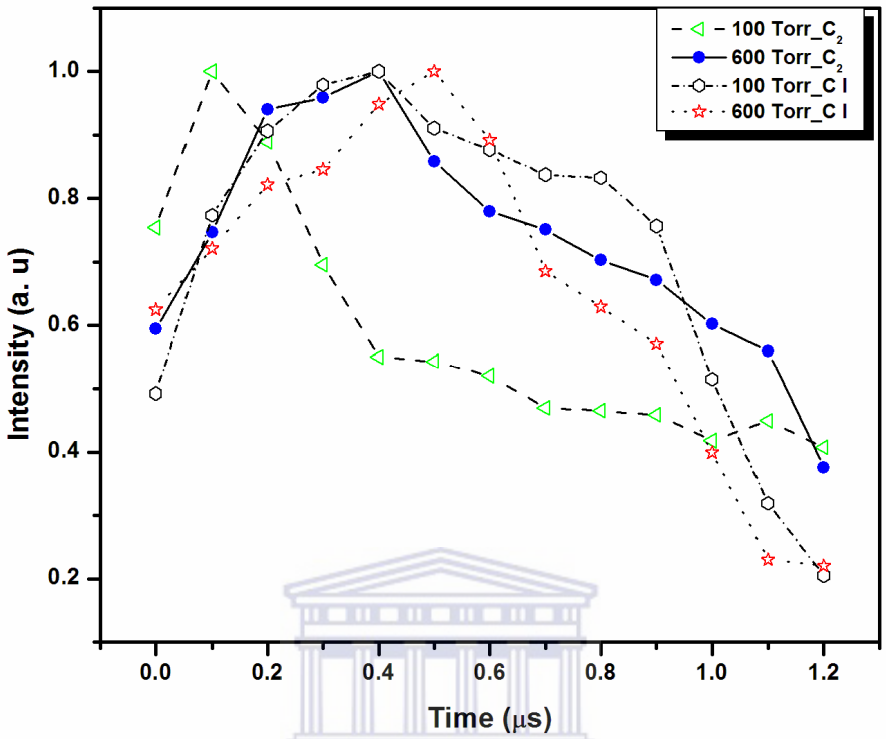

Figure 4.8: Temporal profiles of Swan band and C (I) (247.86 nm) at various argon gas pressures.

4.1.2. The electron temperature and density measurements

At high oven temperature, the electron temperatures from emission lines of a singly ionized C (II) species were determined by applying the Boltzmann distributions law of equation 2.1. Six different line intensities of C (II) as shown in Table 4.2 [4.2] were used. The assumption made was that the plasma was in a locally thermodynamic equilibrium (LTE). This validates the calculations made with the spectral data [4.3]. Figure 4.9 shows the Boltzmann plots employed to deduce the electron temperature. The plots in Figure 4.9 exhibited the linear fit with the correlation coefficients of about 0.99 and 0.98 for 600 and 400 Torr, at the flow rate of 200 sccm. The corresponding constants of the spectral lines employed are obtained from National Institute of Standards and Technology (NIST) data [4.2]. The plotted data are not

spread throughout the linear fit. This was because the wavelengths of the strong C (II) emission lines lie predominantly in the upper energy level between 16.0 eV and 16.5 eV and between 18.5 and 19.0 eV. The behaviour of the plot is consistent with the published data by Harilal *et al*. [4.4] and Hermann *et al.* [4.5].

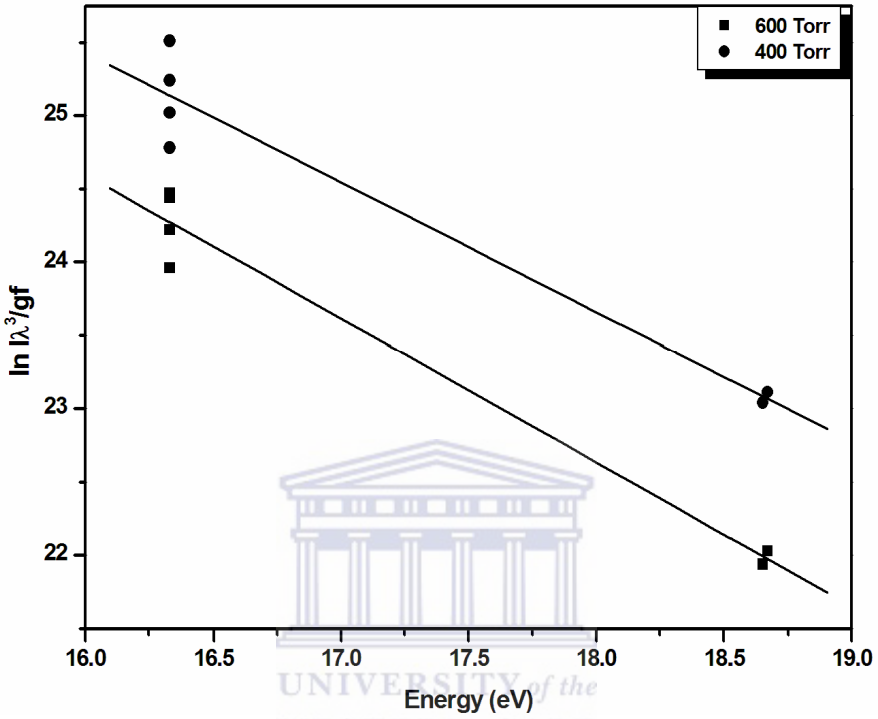

Figure 4.9: Boltzmann plot used for estimating the temperature of the plasma at 500 ns, at a distance of 1 mm from the target and the pressures of 400 and 600 Torr and flow rate of 200 sccm.

Table 4.2: Parameters used related to the 6 wavelength employed to analyse the plasma emission [4.2].

Wavelength (nm)	Upper energy level E_2 (eV)	Oscillator strength f_{ik}	Upper level statistical weight $g_2=2j+1$
250.9	18.67	0.09	4
251.3	18.65	0.08	6
283.7	16.33	0.10	4
657.9	16.33	0.47	4
723.3	16.33	0.50	4
723.8	16.33	0.55	6

The FWHM of the Stark broadened lines was used for the estimation of electron density (in cm^{-3}) through the relation shown in equation 2.5 [4.3]. Figure 4.10 shows the experimental data fitted with a Lorentzian. The data represent the Stark broadened profile of C (II) obtained at 283.7 nm at distance of 3 mm from the target surface at the pressure of 400 Torr, the flow rate of 200 sccm and the delay time of 500 ns.

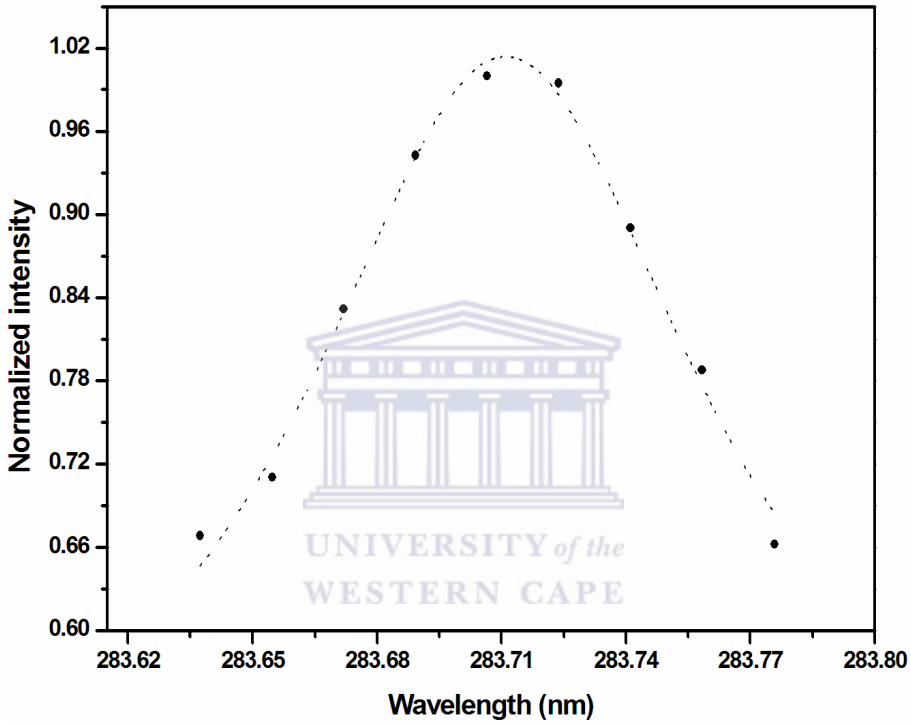

Figure 4.10: Stark-broadened profiles of C (II) lines at the wavelength of 283.7 nm and at 5 mm distance from the target surface. The smooth curves represent the Lorentzian profile fit on the experimental data.

4.1.3. Spatial and temporal evolution of the electron temperature and density

Figure 4.11 (a-d) shows the spatial profile of electron temperature[1] obtained at 1000 °C and at the pressures of 400 Torr, 600 Torr and at a fixed Ar flow rate of 200 sccm. In (a) and (b), an electron temperature decreases slowly with distance, especially at a distance less than 2 mm. The steeper decrease in temperature between 2 and 5 mm is probably due to the rapid conversion of thermal energy into kinetic energy close to the target with plasma attaining its maximum expansion velocities as its expands. However, in (c) and (d), the electron temperature decreases much more rapidly at shorter distances from the target surface. The rapid decrease in temperature can be attributed to the increase in pressure which increases the confinement of the plasma in the vicinity of the target surface caused by an increase in frequency of electron collisions with background gas atoms [4.6]. The electron temperature in the region between 2 mm and 5 mm levels off. The Variation of electron temperature in (b) and (d) with distance (z) approximately follows $z^{-0.3}$ and z^{-2}. This appears to be closer to the optimum condition for carbon nanotubes (CNTs) synthesis, to be discussed later in section 4.2 below. These plots of distance versus electron temperature of a plasma plume are consistent with other studies [4.7] and [4.4].

[1] 1 K ≈ 11604.45 * eV

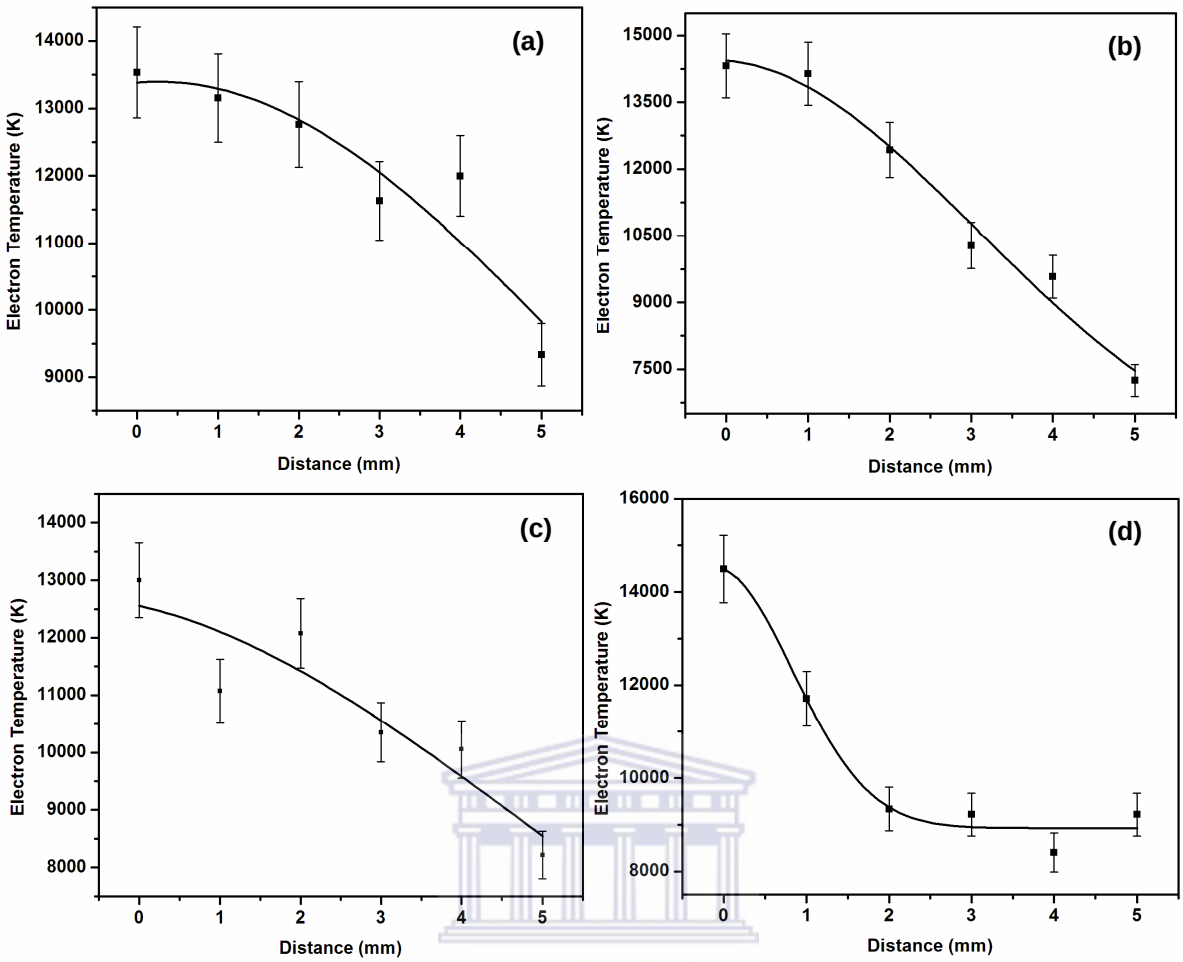

Figure 4.11: Variation of electron temperature as a function of distance from the target surface: (a) 400 Torr, 150 sccm; (b) 400 Torr, 200 sccm; (c) 600 Torr, 150 sccm, and (d) 600 Torr and 200 sccm, recorded at 500 ns gate delay.

The temporal profiles of the electron temperature and density are shown in Figure 4.12 (a) and (b) at the pressure of 400 Torr and Ar flow rate of 200 sccm, recorded at a 0 mm distance from the target surface. It is clear that near the target surface the electron temperature and density attains their maximum value and then decreases with time due to the expansion of the plume. Close to the target, the initial electron temperature and density were measured to be 16 330 K and 2.15×10^{17} cm^{-3}. In its initial phase, during the time a single laser pulse interacts with the surface, the plasma expands isothermally. Once the pulse is extinguished, the electron temperature and density decreases rapidly with time, since no more energy is added into the plasma. Therefore, the thermal energy is converted into kinetic energy and the

plasma cools through the process of adiabatic expansion and the expansion velocities at the temperatures of 16 330 K and 12 166 K are 3.75×10^4 cm.s^{-1} and 3.2×10^4 cm.s^{-1}, respectively. Between the time delay of 0.7 μs and 0.9 μs, the electron temperature increases with time. A slight increase in electron density was also noted at 0.8 μs and 0.9 μs. The onset of recombination processes starts after 500 - 600 ns. The formation of higher carbon systems such C_2 lead to energy being released. This energy can be the reason for the short increase of electron temperature.

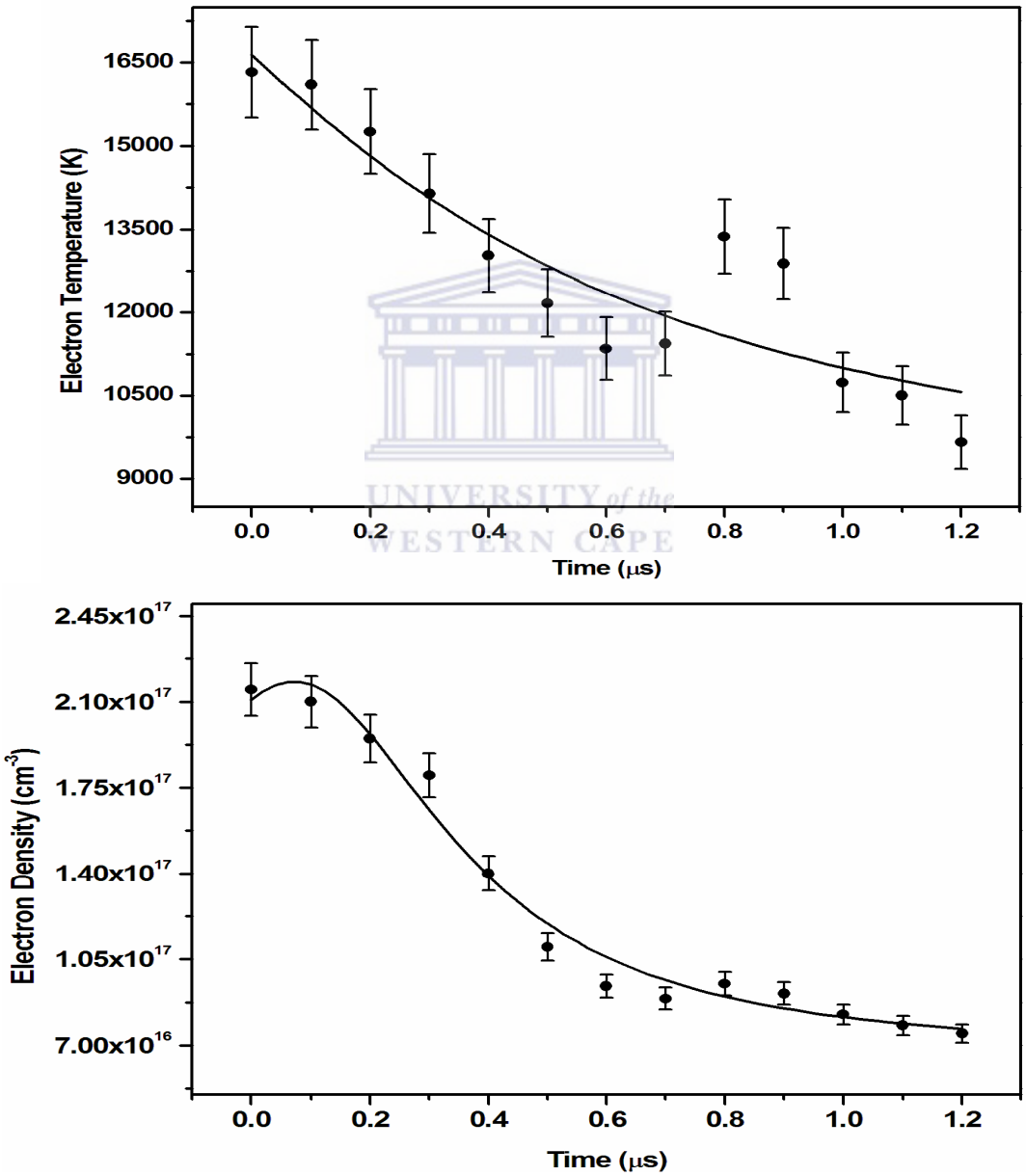

Figure 4.12: Temporal evolution of electron temperature and density at 400 Torr and Ar flow rate of 200 sccm, recorded at 0 mm distance from the target surface.

Figure 4.13 shows the electron density as a function of distance from the target surface; in a time delay of 500 ns. The results in (a) and (b) show that initially, the electron density has its maximum values of 1.22×10^{17} and 1.4×10^{17} cm^{-3} at a distance of 0 mm and decreases to 1.33×10^{17} cm^{-3} and 1.14×10^{17} cm^{-3}. It can be seen that the decay of the electron density is slightly slower at shorter distances i.e. <2 mm. But after 2 mm the decay is much faster. Thereafter, it levels off. The rapid decrease in electron density at 2 mm onwards is because of the adiabatic plasma expansion, recombination and diffusion that exist within the plasma volume. In (c) and (d) there is a rapid decreasing trend in electron density which is caused by the increase in Ar pressure [4.6]. Spatial dependence of electron density in (a-d) appears to follow approximately z^{-1} relation which indicates that the initial expansion is one dimension. These results are in good agreement with the predictions of the plume expansion model given by Singh and Narayan [4.8]. In addition, the obtained results on electron density are consistent with the ones obtained by Harilal *et al*. [4.4, 4.7, and 4.9].

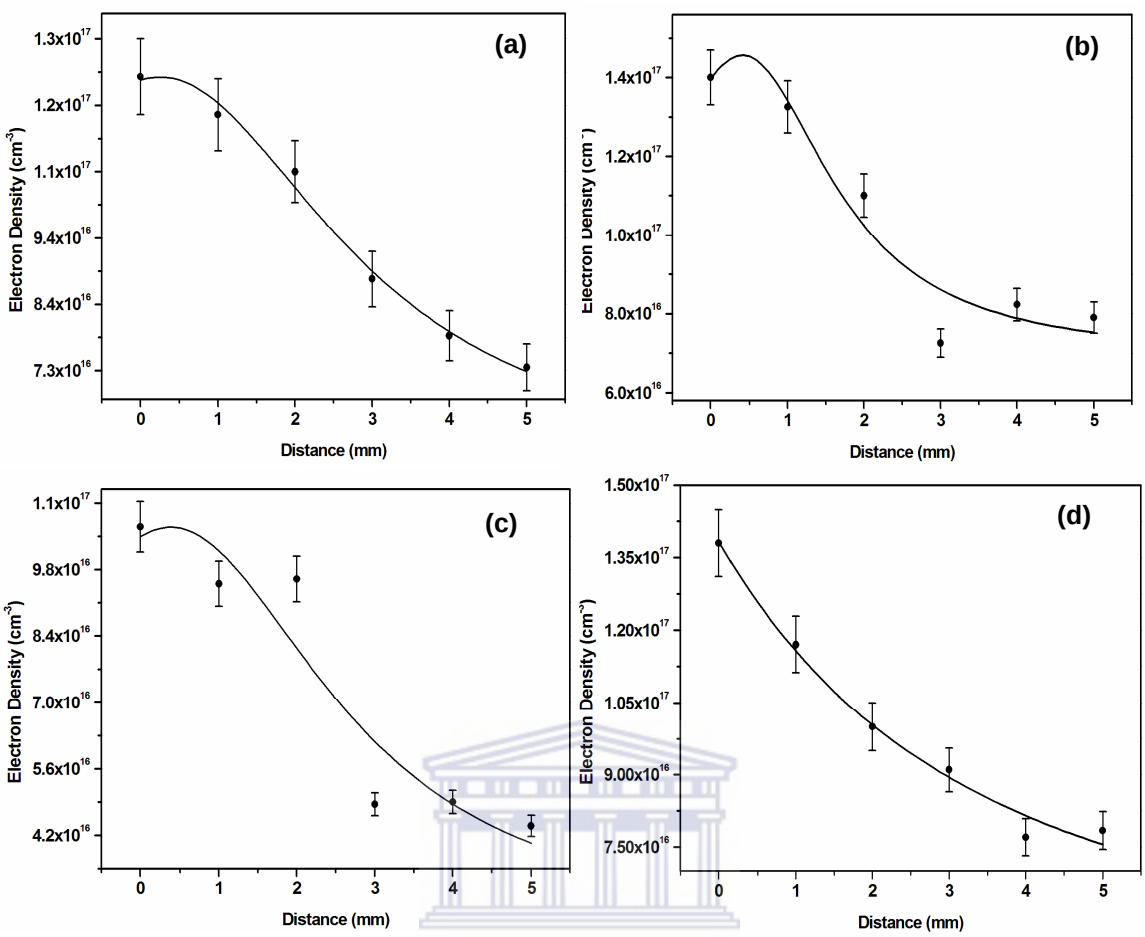

Figure 4.13: Spatial evolution of electron density recorded at different pressures and flow rates: (a) 400 Torr, 150 sccm; (b) 400 Torr and 200 sccm; (c) 600 Torr, 150 sccm, and (d) 600 Torr and 200 sccm.

4.2. Characterization of CNTs by Raman spectroscopy

Raman spectroscopy measurements were done on as-prepared samples. The main features of Raman spectra of SWCNTs are their D-band vibration mode at $1250 < \omega_D < 1450$ cm^{-1}, which result from sp^2 hybridized carbon domains. The G-band was reported earlier to appear at the frequencies between $1500 < \omega_G < 1600$ cm^{-1}. The radial breathing mode (RBM) of the tubes was also reported in chapter three to be a unique feature of SWCNTs. Since its only appears in SWNCTs. From this feature, the carbon nanotube diameter can be determined. In Figure 4.14(a), the RBM for the

Raman spectra of SWCNTs synthesized at pressures of 100, 400 and 600 Torr, and at flow rate of 150 sccm are shown in Table 4.3. Using equation 3.6, the tubes diameters (d_t) probed by 514.5 nm (2.4 eV) radiation were calculated and they are shown in Table 4.3. Raman spectra at 100 Torr and 150 sccm are shown in Figure 4.14(a). Here, the intensity of the D-band is higher; hence it indicates a higher concentration of defects within the tubular walls of SWCNTs. However, at 400 Torr and 150 sccm, the intensity of the D-band is slightly lower as compared to 600 Torr, indicating the synthesis of better quality of SWCNTs.

The G mode has two features which are the lower G frequency (G^-) and the upper G frequency (G^+). The values for the lower frequency G^- and the upper frequency G^+ are shown in Table 4.3. Figure 4.14(b) shows the Raman spectra of SWCNTs deposited at Ar pressure of 100, 400 and 600 Torr and flow rate of 200 sccm. In this spectra, the RBM for all the pressures was found to be around 185.0 cm^{-1} meaning that the tube diameters were roughly the same as those obtained at the flow rate of 150 sccm. These values are tabulated in Table 4.3. At 301.8 and 888.7 cm^{-1}, there are two peaks observed which are attributed to the substrate. The high intensity of D-band observed at 100 Torr, in Figure 4.14 confirms the low quality SWCNTs. The SEM micrographs of the sample synthesized at 100 Torr is shown in section 4.3 and in Figure 4.17. It also confirms the poor quality of the material synthesized at 100 Torr. A broad low intensity of the D-band observed at 400 Torr and 200 sccm is indicative of high quality SWCNTs. At the pressure of 400 Torr, optimum confinement in the vapour plume appears to have been achieved. These results are in agreement with the results observed by Smalley *et al* [4.10] and also in agreement with the ones observed by Moodley *et al*. [4.11] using different percentages of Ni/Co as catalysts.

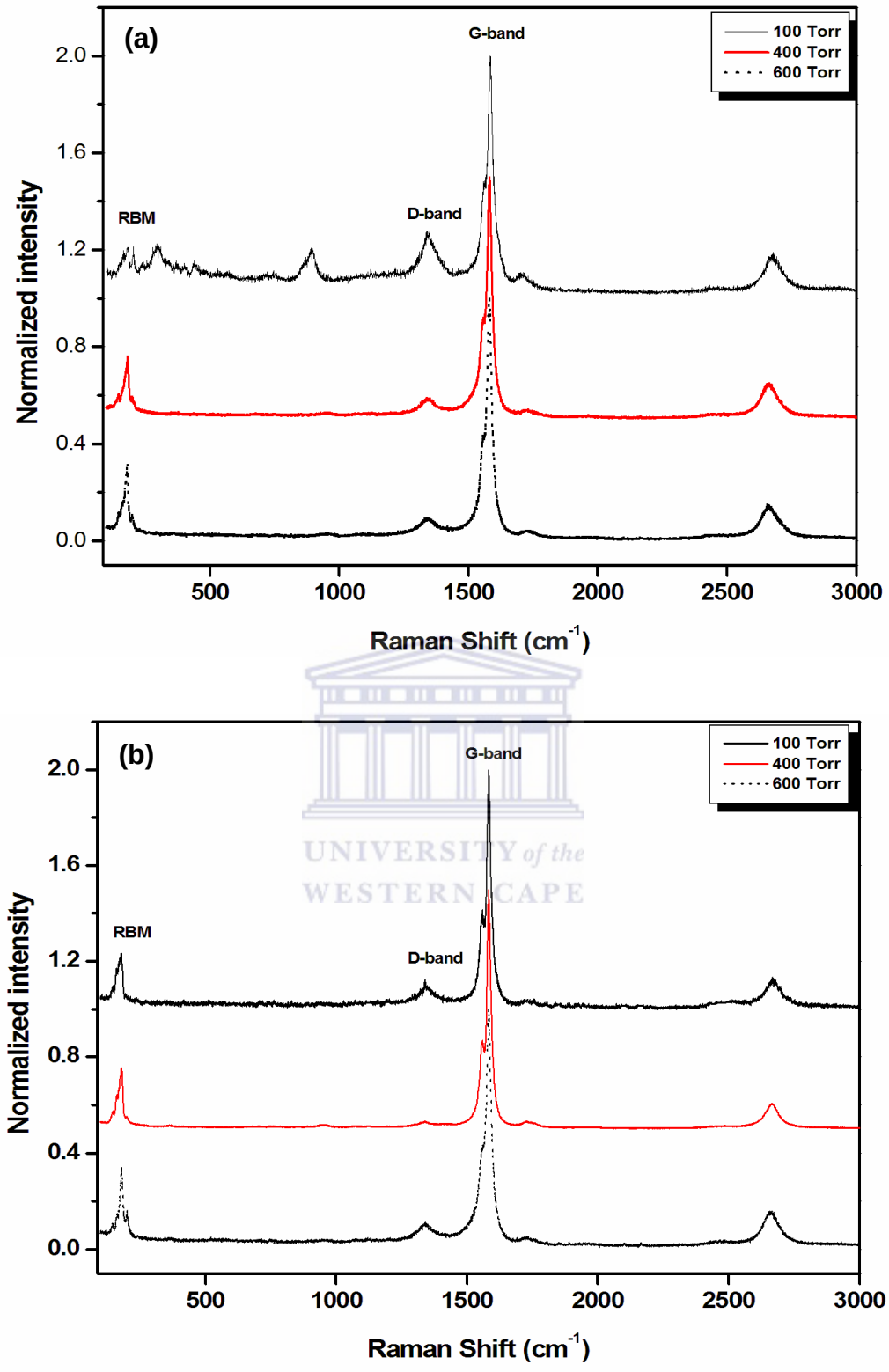

Figure 4.14: Raman Spectra of semiconducting SWCNTs in the samples, synthesized at different Ar pressures and flow rates: (a) 100 Torr, 400 Torr, 600 Torr; 150 sccm and (b) 100 Torr, 400 Torr, 600 Torr; 200 sccm.

Table 4.3: Raman data probed by a 2.4 eV radiation laser at 150 sccm.

Pressure (Torr)	RBM (cm^{-1})	d_t (nm)	D-band (cm^{-1})	G^+ cm^{-1}	G^- cm^{-1}
100	186.5	1.33±0.03	1340.8	1585.6	1562.3
400	181.4	1.37±0.03	1335.6	1685.6	1548.1
600	181.4	1.37±0.03	1335.6	1685.6	1551.9.

Figure 4.15 shows the Raman spectrum of SWCNTs probed by a 647 nm laser. There are changes in the RBM, D-band and G-bands. The “camel” shaped G-band is indicative of metallic tubes. This means that using an excitation laser of 647 nm, the Raman spectra of the metallic tube content are resonantly enhanced. The RBM band of the material synthesized at 100 Torr shows a broader distribution of tubes with different diameters. The nanotube diameters for material synthesized at 100, 400 and 600 Torr and the flow rate of 150 sccm measured at 647 nm laser excitation are shown in Table 4.4. The increase in the D-band intensity at 100 and 600 Torr is indicative of a higher concentration of defects in SWCNTs. Furthermore, by looking at the relative intensities of the D-and G-bands in Figure 4.14 and 4.15, it can be seen that the materials synthesized at 100 Torr have more defects. In general, metallic tubes have high concentration of defects than semiconducting nanotubes.

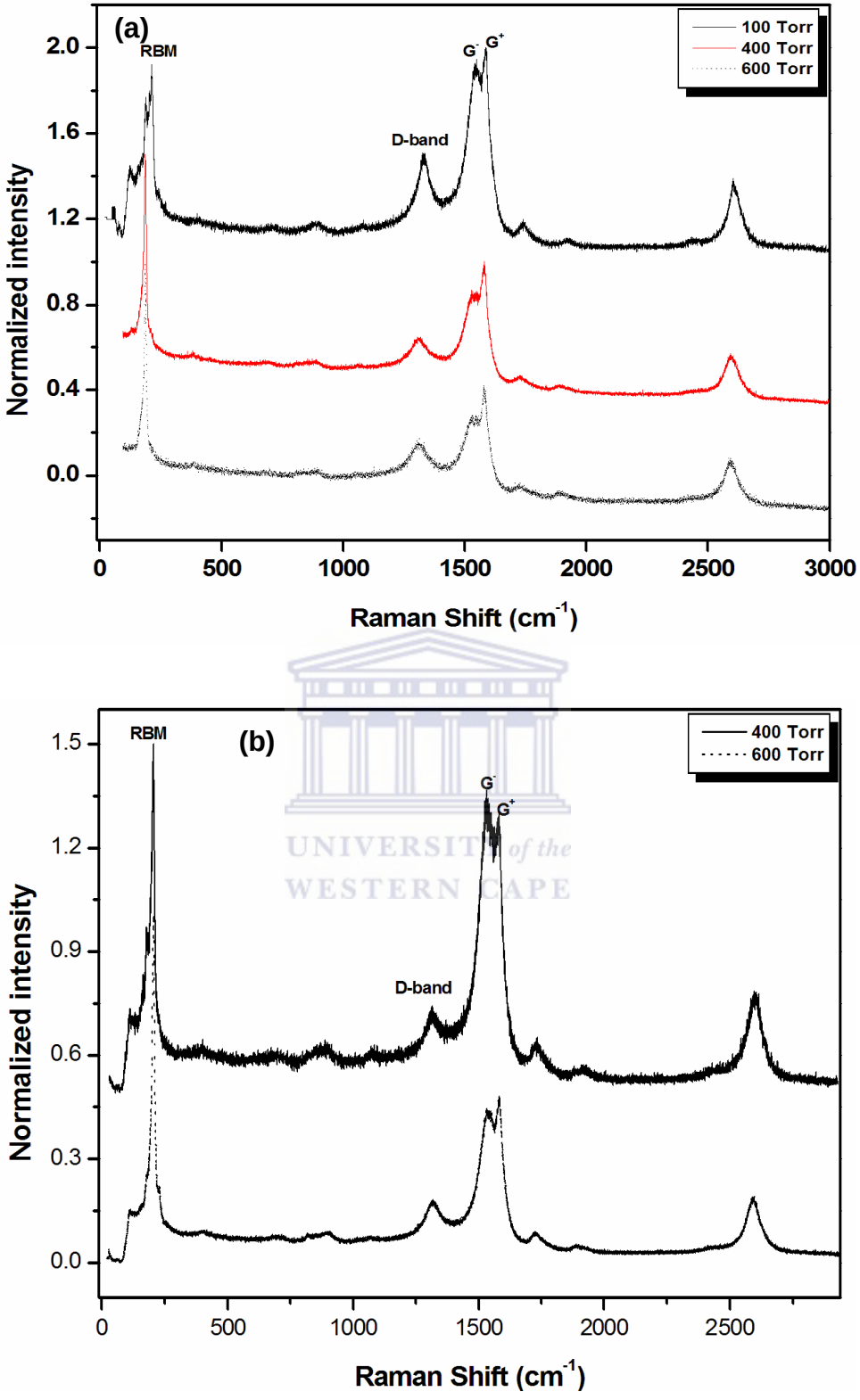

Figure 4.15: Raman spectra of SWCNTs probed by a 647 nm laser excitation, at 100, 400 and 600 Torr: (a) Ar flow rate of 150 sccm and (b) Ar flow rate of 200 sccm.

Table 4.4: Summary of Raman spectra of SWCNTs probed by a 647 nm laser at a fixed flow rate of 150 sccm.

Pressure (Torr)	RBM (cm^{-1})	d_t Range (nm)	D-band (cm^{-1})
100	217.1	(1.14- 2.01) ±0.03	1331.4
400	187.8	(1.32-2.14) ±0.03	1307.6
600	187.8	(1.32-2.14) ±0.03	1312.3

4.3. Characterization of CNTs by SEM

The scanning electron microscopy images of samples prepared from laser ablation of a graphite target mixed with a 4% Y and 1% Ni are shown in Figure 4.16 and 4.17. The flow of Ar gas was monitored at different flow rates and pressures while the furnace temperature was set at 1000 ^{0}C. The synthesized materials were scraped off as thin films coated on the inside walls at the end of the outer quartz tube. The SEM studies on these samples reveal a very high yield of SWCNT under argon gas at a pressure of 400 Torr and at the flow rates of 150 and 200 sccm. These micrographs are shown in Figure 4.16(a) and (b). The high yield is probably due to the fact that the Ar pressure between 200 and 400 Torr and the flow rate of 150 and 200 sccm restrict the expansion of the vapour plume thereby reduces the rapid decrease in a temperature of the plasma plume due to adiabatic expansion. These results are in good agreement with that reported by Smalley *et al*. [4.9]. At 600 Torr irrespective of the flow rates, the SEM images of Figure 4.16(c) and (d) show

an excess of amorphous carbon and very little amount of tubes. This is probably due to the fact that an increase in a pressure results in high collision probabilities of the evaporated species with the ambient gas molecules and therefore leads to an increase in the cooling rates. This is clearly shown in Figure 4.11(c) and (d), where a sharp drop in electron temperatures was recorded. It was also observed that, at a pressure of 600 Torr, the ablated material travelled forward up along the inner quartz tube. This means that a pressure and flow of the argon gas was insufficient to confine the constituents of the plasma plume i.e. the momentum of the plume was higher than that of argon. In this instance the catalysis action and the condensing of the carbon plasma plume into tubes is reduced. At low pressures of 100 Torr, the situation result in the rapid cooling due adiabatic expansion were an increase in amorphous carbon and graphitic carbon particles was found as shown in Figure 4.17. This correlates very well with OES and Raman spectra of the same sample as shown in Figure 4.14 and 4.15; at 100 Torr. For instance at 400 Torr the decrease in electron temperature was found to decrease more rapidly than at any other pressures and hence at this pressure the Raman spectra revealed a very high yield of SWCNTs.

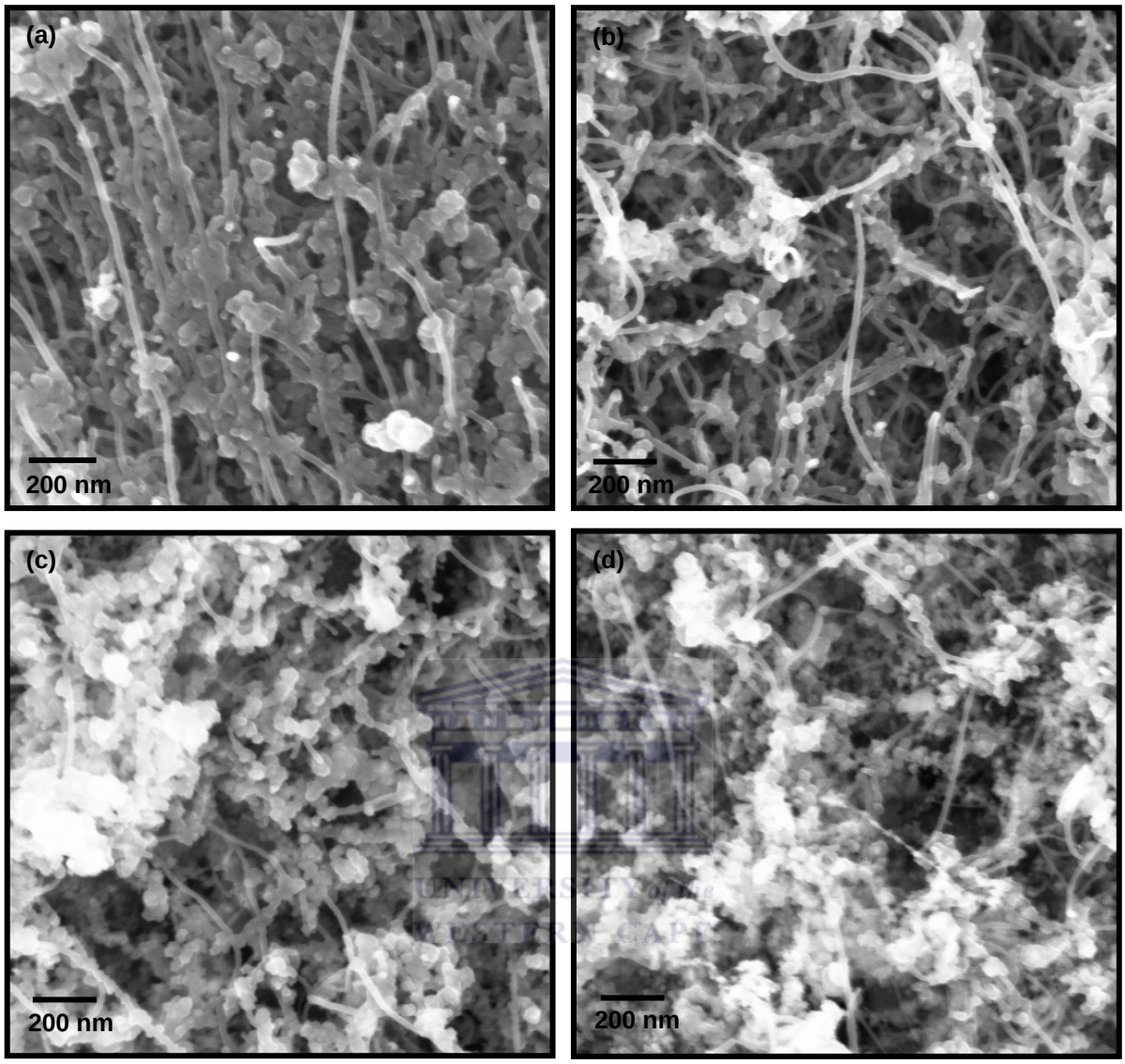

Figure 4.16: (a) SEM images of SWCNTS produced at 1000 ºC; at different pressures and Ar flow rates: (a) 400 Torr 150 sccm, (b) 400 Torr, 200 sccm, (c) 600 Torr, 150 sccm, and (d) 600 Torr, and 200 sccm.

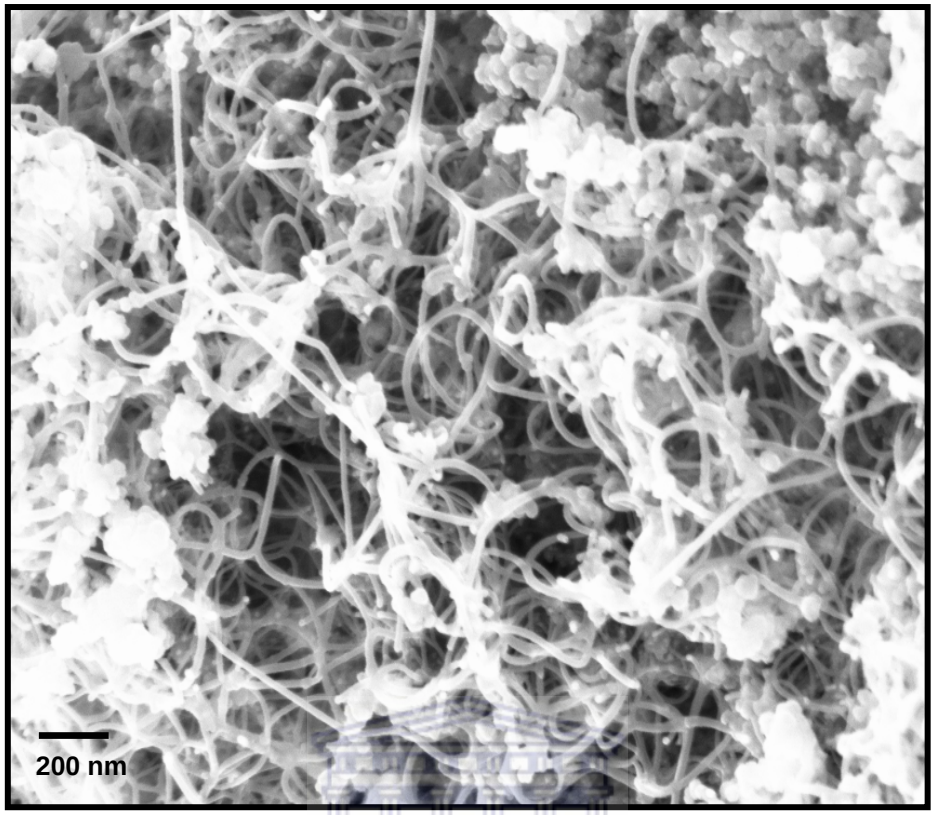

Figure 4.17: SEM image of SWCNTs synthesized at a pressure of 100 Torr and the argon flow rate of 200 sccm.

4.4. References

[4.1] Pearse R. W B and Gaydon A G, (London: Chapman and Hall), **95** 94 (1965).

[4.2] NIST Atomic Spectra Database; http://physics.nist.gov/PhysRefData/ASD/index.html.

[4.3] H. R. Griem, *Plasma Spectroscopy* ~McGraw-Hill, New York, (1964)

[4.4] S. S Harilal, Beau O'Shay, and Mark. S. Tillack, *Journal of Appl. Phys*. **98** 013306 (2005).

[4.5] S. Amoruso, R Bruzzese, N. Spinelli and R Velotta *J. Phys. B: At. Mol. Opt. Phys*. **32** 131 (1991).

[4.6] S. S. Harilal C. V. Bindhu, V. P. N. Nampoori, and C. P. G. Vallabhan *Appl. Phys. Lett., Vol*. **72** No. 2 (1998).

[4.7] S. S. Harilal, C. V. Bindhu, V. P. N. Nampoori, and C. P. G. Villabhan Appl. Spec. **52** 3449 (1998).

[4.8] R. K. Singh, J. Narayan: *Phys. Rev*. B **41** 8843 (1990).

[4.9] S. S. Harilal, C. V. Bindhu, Riju C. Issac, V. P. N. Nampoori, and C. P. G. Vallabhan, J. *Appl. Phys*. **82** (5) (1997).

[4.10] R.E. Smalley: *Acc. Chem. Res*. **25** 98 (1992).

[4.11] M.K. Moodley, N. J Coville, B. C Holloway and M. Maaza, *South African Journal of Science*. **102** 364 (2006).

CHAPTER FIVE

5.1. SUMMARY

Spontaneous emission spectra of the plasma plume were obtained by ablating a graphite composite target in argon gas. The effect of Ar gas on the plume is reported and it was noticed that Ar gas increases the plume confinement with the increasing pressure. This also enhances the emission spectra of plume species such as CI, CII, etc. However, the Y and Ni present in the graphite target were found to be dominating in the entire spectra at lower Ar pressures irrespective of the flow rates. At higher pressures, the intensity of Y and Ni decreases while the intensity of Ar was increasing. Moreover, the C_2 Swan band ($d^3\Pi g \rightarrow a^3\Pi u$) and Deslandres D' Azambuja bands ($C^1\Pi_g$ - $A^1\Pi_\mu$) intensity were observed. The C_2 Swan bands were dominating at most pressures over the C_2 Deslandres. The C_3 emission band which was expected to appear at wavelength of 400 nm in the spectrum was not observed. The Y and Ni were identified to be contributing to the increase of the C_2 intensity, since that they were overlapping. That is, their wavelengths are almost in the same range where the C_2 wavelength appears, and hence the effect is the strong influence on the band intensity of one species (e.g. C_2) by the presence of the other such as Ni or Y.

The analyses on the time and space resolved measurements on electron temperature and electron density were done by using Boltzmann equation and by making use of the full width half maximum FWHM $\Delta\lambda_{1/2}$ of the Stark broadening profile of a particular carbon emission lines. In this analysis emission lines of a singly ionized CII at various pressures and flow rates were made. At 400 and 200 sccm the spectroscopic measurements on the Stark

broadened profiles were found to be approximately Lorentzian. The experimental curve shown in Figure 4.10 fitted fairly well with a typical Lorentzian profile. At the pressure of 400 Torr and flow rates of 150 and 200 sccm, and furnace temperature of 1000 ºC, as shown in Figure 4.11, the rate of decrease in electron temperature was lower than at a pressure of 600 Torr as a function of distance from the target. At 600 Torr, the electron temperature decreases rapidly at shorter distances irrespective of the flow rates because of the increase in Ar pressure. The increase of a pressure increases the confinement of the plasma close to the target surface. The frequency of electron/ion collisions with the background gas atoms increases with an increase in pressure. At 400 Torr and 200 sccm the temporal profiles of the electron temperature and density were recorded as shown in Figure 4.12. It was noticed that near the target surface the temperature and density attain their maximum value and then decreases with time due to the adiabatic expansion of the plume. In the vicinity of the target the initial electron temperature and density of about 16 330 K and 2.15 $\times 10^{17}$ cm^{-3} were observed. In its initial phase, during the time a single laser pulse interacts with the surface, the plasma expands isothermally. Once the pulse is extinguished, the electron temperature and density decreases rapidly with time, since no more energy is added into the plasma. Therefore, the thermal energy was converted into kinetic energy and the plasma cooled through the process of adiabatic expansion. At temperatures of 16 330 K and 12 166 K the expansion velocities were measured to be about 3.75×10^{4} and 3.2×10^{4} $cm.s^{-1}$.

For carbon nanotube growth, a pressure of 400 Torr, and electron temperatures ranging from 10 000 K to 14 500 K were found to be favourable as shown in Figure 4.11. Optical emission line intensity measurements associated with C_2 Deslandres D' Azambuja, Nickel and Yttrium at 400 Torr and 200 sccm are shown in Figures 4.3 - 4.5, respectively. A decaying oscillatory behaviour of the intensities is clearly evident. There appears to be some correlation at turning points in the graph and nanotube growth. At the pressure of about 400 Torr, C_2, Y and Ni are more excited especially at shorter distances as compared to 600 Torr. This shows that at this pressure

the optimum confinement in the vapour plume is achieved. Hence, this pressure provides the most suitable temperature and concentration conditions of evaporated species (materials) leading to high SWCNTs yields. However, at 100 Torr, initially the C_2, Y and Ni are more excited than at 400 Torr. However, due to a low pressure, the plume expansion is long; the C and metal particles (Ni, and Y) could not mix homogeneously or completely due to an increased in a cooling rate to the materials. At 600 Torr the intensity of C_2, Y and Ni is low. At this pressure, the amount of evaporated material is less than at the lower pressures and explains the lower intensity in the elemental lines as shown in Figure 4.6 and 4.7 where the C_2 Swan bands intensity was low at this pressure. The quality of the materials collected at 600, 400 Torr, etc are corroborated by Raman and SEM which show the presence of CNTs in the samples. However, the amount of material collected was highest at 400 Torr and this corresponds directly to the regime where C_2 intensities, the precursors to nanotubes, are highest. The low quality of nanotubes obtained at 600 Torr is related to the rapid decrease in temperatures observed in OES of Figure 4.11 (c) and (d). The rapid decrease in temperature is attributed to the increase in pressure, because as pressure increases, the confinement of the plasma close to the target surface takes place, which in turn increases the effective frequency of electron collisions with a background gas. As a result there is a reduction in plasma lifetime. This reduction lowers the probability of SWCNTs being formed where high sustained temperatures are favourable. Lastly, at low pressure such as 100 Torr, the plume was found to be expanding too rapidly leading to an increased cooling rate for evaporated species and resulting in a low SWCNTs yield and higher amorphous carbon content. Again, at higher pressures, sustained high temperature plasma is not achieved.

In general, we observed that a pressure of 400 Torr and a flow rate of 200 sccm provide the most suitable conditions for synthesis of SWCNTs. This was confirmed by Raman spectroscopy, SEM and OES. The slow trend decrease in temperature which is suitable for evaporation of carbon material was observed in OES as shown in Figure 4.11.